AGU PUBLICATIONS

JGR

Journal of Geophysical Research: Atmospheres

RESEARCH ARTICLE
10.1002/2015JD023303

Key Points:
- In situ OPC stratospheric aerosol measurements corrected for a calibration error
- Corrected OPC and SAGE II stratospheric aerosol extinctions are in agreement
- In nonvolcanic periods, OPC and SAGE II surface areas are in agreement

Correspondence to:
M. Kovilakam,
mundakkaramv@ornl.gov

Citation:
Kovilakam, M., and T. Deshler (2015), On the accuracy of stratospheric aerosol extinction derived from in situ size distribution measurements and surface area density derived from remote SAGE II and HALOE extinction measurements, *J. Geophys. Res. Atmos.*, *120*, doi:10.1002/2015JD023303.

Received 27 FEB 2015
Accepted 21 JUL 2015
Accepted article online 24 JUL 2015

On the accuracy of stratospheric aerosol extinction derived from in situ size distribution measurements and surface area density derived from remote SAGE II and HALOE extinction measurements

Mahesh Kovilakam[1,2] and Terry Deshler[2]

[1]Now at Oak Ridge National Laboratory, Oak Ridge, Tennessee, USA, [2]Department of Atmospheric Science, University of Wyoming, Laramie, Wyoming, USA

Abstract In situ stratospheric aerosol measurements, from University of Wyoming optical particle counters (OPCs), are compared with Stratospheric Aerosol Gas Experiment (SAGE) II (versions 6.2 and 7.0) and Halogen Occultation Experiment (HALOE) satellite measurements to investigate differences between SAGE II/HALOE-measured extinction and derived surface area and OPC-derived extinction and surface area. Coincident OPC and SAGE II measurements are compared for a volcanic (1991–1996) and nonvolcanic (1997–2005) period. OPC calculated extinctions agree with SAGE II measurements, within instrumental uncertainty, during the volcanic period, but have been a factor of 2 low during the nonvolcanic period. Three systematic errors associated with the OPC measurements, anisokineticity, inlet particle evaporation, and counting efficiency, were investigated. An overestimation of the OPC counting efficiency is found to be the major source of systematic error. With this correction OPC calculated extinction increases by 15–30% (30–50%) for the volcanic (nonvolcanic) measurements. These changes significantly improve the comparison with SAGE II and HALOE extinctions in the nonvolcanic cases but slightly degrade the agreement in the volcanic period. These corrections have impacts on OPC-derived surface area density, exacerbating the poor agreement between OPC and SAGE II (version 6.2) surface areas. This disparity is reconciled with SAGE II version 7.0 surface areas. For both the volcanic and nonvolcanic cases these changes in OPC counting efficiency and in the operational SAGE II surface area algorithm leave the derived surface areas from both platforms in significantly better agreement and within the ±40% precision of the OPC moment calculations.

1. Introduction

Accurate estimation of stratospheric aerosol surface area density (SAD), from various stratospheric measurements, is important because of the impact of the aerosol on radiation [*Minnis et al*., 1993; *Ridley et al*., 2014] and because of chemical reactions on the surface of the particles, which subsequently affect the abundances of oxides of nitrogen and ozone, and thereby the chemistry of the stratosphere [*Hofmann and Solomon*, 1989; *Rodriguez et al*., 1991; *Fahey et al*., 1993; *Solomon et al*., 1996]. Global atmospheric chemical models thus require an aerosol surface area climatology. For this, the satellite extinction records of the Stratospheric Aerosol and Gas Experiment (SAGE) II, and to some extent, the Halogen Occultation Experiment (HALOE) are used to derive aerosol SAD [*World Meteorological Organization*, 2003]. During nonvolcanic periods, however, the satellite-derived SADs have not agreed with in situ measurements [*Deshler et al*., 2003a; *Stratospheric Processes and their Role in Climate* (*SPARC*), 2006; *Reeves et al*., 2008].

Previous comparisons of SAD between University of Wyoming balloon-borne optical particle counter (OPC) and satellite measurements show that during nonvolcanic periods, SAGE II SADs (version 6.0) were lower than those derived from both HALOE and OPC measurements with the difference about a factor of 2 (*Hervig and Deshler* [2002], SAGE II version 6.0; *Deshler et al*. [2003a], SAGE II version 6.1). *Reeves et al*. [2008] compared SAGE II (version 6.2) extinction, SAD, and volume density with the University of Denver's in situ measurements using a focused cavity aerosol spectrometer (FCAS). Their results showed that extinctions agree, within instrumental uncertainties, except at 0.386 μm below 17 km; however, SAGE II SAD is lower than FCAS by a factor of 1.5 to 3.0, similar to the OPC-SAGE II comparisons. This difference in aerosol surface area density is large enough to be significant for stratospheric chemistry. A change in SAD from about 1 $\mu m^2\,cm^{-3}$ to about 4 $\mu m^2\,cm^{-3}$ increases the ozone loss rate by about 25% [*Solomon et al*., 1996].

However, in this study, we find that SAGE II (version 7.0) SADs [*Thomason et al*., 2008] and the SAD derived from the corrected OPC measurements are in quite good agreement.

For the study here, OPC measurements are compared with SAGE II measurements because the remarkable SAGE II measurement period (October 1984 to August 2005) provides the most comprehensive global stratospheric aerosol record, covering both volcanic (following the 1991 Pinatubo eruption) and nonvolcanic periods, and is thus the stratospheric aerosol climatology most commonly used in chemical models, even though there are questions about the accuracy of SAGE II SADs during volcanically quiescent periods. Such questions prompted *Thomason et al*. [2008] to provide an alternate method to calculate SAGE II SAD. SAD calculated using this method is what is currently in the SAGE II (version 7.0) climatology. Further to broaden the comparison basis, OPC measurements are also compared with HALOE measurements since HALOE also contributes to the stratospheric aerosol record during both volcanic and nonvolcanic periods and provides a second independent comparison to the OPC measurements.

The primary measurement of SAGE II is extinction, from which SAD is calculated. Thus, any comparison with SAGE II must begin with a comparison of aerosol extinction. Previous comparisons of extinction between OPC and SAGE II measurements [*Hervig and Deshler*, 2002; *Deshler et al*., 2003a, 2006] show that during the nonvolcanic period, the OPC-derived extinctions are lower than SAGE II and HALOE extinctions. This discrepancy in extinction between the OPC and SAGE II, particularly during background periods, led to the investigation here of uncertainties and systematic errors associated with the Wyoming OPC measurements.

2. Wyoming Optical Particle Counter

The University of Wyoming balloon-borne OPC was developed by *Rosen* [1964], applied to global [*Hofmann et al*., 1975], volcanic [*Hofmann and Rosen*, 1983], and long-term [*Hofmann*, 1990] stratospheric aerosol measurements, before being modified for larger particle, polar stratospheric cloud measurements [*Hofmann and Deshler*, 1991]. The instrument illuminates particles in air flowing through a sample chamber using white light and measures forward scattering from particles as they pass through the focal point of a darkfield microscope. The intensity of light scattered from individual particles is measured with a pair of photomultiplier tubes. The pulse height measured is related to particle size. The number concentration is determined from the count rate of the photoelectric pulses and the flow rate of air through the chamber. Mie theory is used to determine the instrument response as a function of particle size. The counter response is calculated as a function of scattering angle, particle index of refraction, particle size, and the energy and wavelength of the incident radiation [*Hofmann et al*., 1975; *Deshler et al*., 2003a]. Although the theoretical counter response function provides the relative characteristics of the OPC as a function of size, the absolute response is set by calibrating each gain stage of the instrument using monodispersed polystyrene latex spheres with a refractive index of 1.59.

The counter developed by Rosen was used to initiate the Wyoming stratospheric aerosol record in 1971 [*Hofmann et al*., 1975]. Particles in the size range 0.15–0.25 μm in radius were measured through the early 1990s [*Hofmann*, 1990] using detectors aligned at 25° in the forward direction, hereafter referred to as an OPC_{25}. This scattering angle limited the monotonic response of the counter to particles < 0.3 μm radius. Mie resonances appear in the counter response function at larger sizes leading to ambiguity between pulse height and particle size. For the modified OPC [*Hofmann and Deshler*, 1991] the scattering angle of the detector axis was increased from 25° to 40° to remove the nonmonotonic region in the counter response curve, allowing measurements in the size range from 0.15 to 2.0 μm. The flow rate of this instrument, hereafter OPC_{40}, was increased from 1 to 10 L min^{-1}, and the number of channels increased from 2 to 12. OPC_{40}s have been in use in Laramie, Wyoming, since 1990 [*Deshler et al*., 2003a]. The optimum concentration range is 6×10^{-4} to 10 cm^{-3}. To obtain a complete size distribution, a companion condensation nuclei (CN) counter is used to simultaneously measure the concentration of particles greater than 0.01 μm by forcing the particles to grow to an optically detectable size using a growth chamber [*Rosen and Hofmann*, 1977; *Campbell and Deshler*, 2014].

The OPC measurements have random uncertainties in measured size and concentration. The concentration uncertainty is primarily defined by Poisson counting statistics. With a known flow rate (F), measured concentration (N), and sample frequency (S), the Poisson error fraction in terms of concentration can be

written as $(N \cdot F/S)^{-0.5}$. The sample frequency is 0.1 Hz, and the sample flow rate is 167 $cm^3\,s^{-1}$, leading to concentration uncertainties of 85, 25, and 8% for concentrations of 0.001, 0.01, and 0.1 cm^{-3} for an OPC_{40}. These uncertainties would increase by $\sqrt{10}$ for an OPC_{25}. Sizing uncertainties are measured to be about ±10% [*Miao*, 2001; *Eidhammer et al*., 2008], primarily due to pulse width broadening of the photomultiplier tubes.

Stratospheric aerosol size distributions can be approximated using lognormal distributions [*Pueschel et al*., 1992, 1994; *Deshler et al*., 2003a], and there is some experimental evidence for undisturbed aerosol distributions to relax through coalescence to a Gaussian distribution in logarithm space [*Granqvist and Buhrman*, 1976]. Therefore, OPC data are fit with either unimodal or bimodal lognormal size distributions [*Jäger and Hofmann*, 1991; *Hofmann and Deshler*, 1991; *Deshler et al*. 1993, 2003a]. The fitted size distributions are either unimodal or bimodal depending on the number of independent measurements of size and concentration and on which distribution provides the minimum error when compared with the measurements. A unimodal distribution is the only option if there are less than five independent concentration measurements. If there are five or more concentration measurements, then the fitting algorithm will choose between the optimum unimodal and optimum bimodal distribution, depending on which deviates the least from the measurements [*Deshler et al*., 2003a]. The random uncertainties in the measurement of concentration and size control the uncertainties in size distribution parameters and in aerosol moments. These latter overall random uncertainties were estimated using a Monte Carlo simulation and found to be ±30% for size distribution parameters and ±40% for aerosol moments [*Deshler et al*., 2003a].

2.1. Corrections to OPC Measurements

Work up to now has not formally addressed possible systematic errors in OPC aerosol size and concentration measurements. This is in part due to relatively good agreement with satellite extinction measurements during periods with volcanic aerosol loading [*Russell et al*., 1996; *Hervig and Deshler*, 2002], with simultaneous remote aerosol lidar and in situ backscatter measurements [*Adriani et al*., 1995; *Deshler et al*., 2000], and with modeled liquid polar stratospheric cloud volumes from simultaneous in situ measurements of water vapor, nitric acid, and particles [*Deshler et al*., 2003b]. In addition, during the polar stratospheric cloud measurement, described by *Deshler et al*. [2003b], there was good agreement between simultaneous CN concentrations measurements using a CN counter and the concentrations of the smallest OPC channel. All of the CN had been activated as polar stratospheric cloud particles. The common thread underlying these comparisons, not realized until recently, was that they were all done during periods of relatively high stratospheric aerosol load. As will be discovered below, the dominant systematic error investigated here was found to play a significant role only during periods of low aerosol loading.

Three possible systematic errors for the OPC measurements were investigated: evaporation in the particle inlet, anisokineticity, and counting efficiency. These could lead to systematic errors for size due to evaporation or concentration due to counting efficiency and anisokineticity.

2.1.1. Particle Evaporation

The OPC is housed in a styrofoam box, attached to a balloon that rises at an average rate of 5 $m\,s^{-1}$. The aluminum inlet used for sampling the air is aligned vertically with one section of the inlet exposed to the ambient air and the remaining section inside the box. Although the OPC inlet is insulated from the warm optical chamber, the thermal isolation is not complete, and the inlet tube is warmer than the surrounding air. As the ambient air enters the inlet the air temperature will increase from contact with the inlet walls. This may lead to evaporation of water from the aerosol particles during the 16 ms required for the particle to pass from outside to the optical chamber. Evaporation of particles in a purposely heated inlet was analyzed by *Eidhammer and Deshler* [2005] for a study of polar stratospheric cloud particles. The method of Eidhammer and Deshler is used here for the liquid droplets composed of sulfuric acid and water typical of the midlatitude stratosphere. The governing equation for evaporation from a particle is given by [*Pruppacher and Klett*, 1997]

$$r_a \frac{dr_a}{dt} = \frac{D^* M_w}{R \rho_{\text{particle}}} \left(\frac{p_\infty}{T_\infty} - \frac{p_s}{T_a} \right), \tag{1}$$

where r_a is the radius of the particle, M_w the molecular weight of water, R the universal gas constant, ρ_{particle} the density of the particle, p_∞ the ambient partial pressure of water vapor, T_∞ the ambient temperature, and p_s the saturation vapor pressure of water vapor over the solution droplet at the droplet temperature, T_a. The ambient partial pressure of water is calculated using a gas-phase mixing

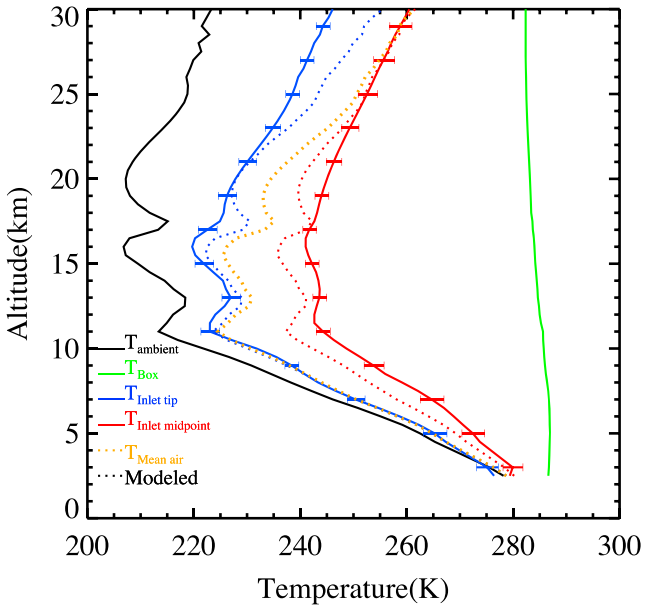

Figure 1. Vertical profiles of measured (solid lines) and modeled (dotted lines) temperatures for an OPC flight. The solid black line is the ambient air temperature, green the measured air temperature inside the instrument box, blue the measured wall temperature at the tip of the inlet, and red the measured wall temperature at 11 cm (midpoint) along the inlet. Modeled mean air temperature is shown as $T_{\text{mean air}}$ in orange. Error bars represent measurement uncertainties.

ratio (which is constant throughout the stratosphere) approximated as 5 ppmv in the stratosphere [*Hofmann and Oltmans*, 1992] and only slowly varies with altitude and time. The modified diffusion coefficient D^* accounts for molecular discontinuities near the particle [*Fuchs and Sutugin*, 1971].

Before equation (1) can be solved, T_a must be found from the heat transfer equation. The rate of sensible heat and mass transfer to a droplet of radius r_a is given by [*Pruppacher and Klett*, 1997]

$$\frac{dQ}{dt} = 4\pi r_a k^* (T_m(x) - T_a) = -4\rho_{\text{particle}} \pi L_v r_a^2 \frac{dr_a}{dt}, \quad (2)$$

where $T_m(x)$ is the mean air temperature in the inlet and is equivalent to T_∞ in (1). With this correspondence and (1) and (2), we get

$$(T_m(x) - T_a) = \frac{D^* w L_v M_w}{R k^*} \left(\frac{p_\infty}{T_m(x)} - \frac{p_s}{T_a} \right), \quad (3)$$

where k^* is the modified thermal conductivity, w the mass fraction of water in the particle, and L_v the latent heat of vaporization. The density of the particle is also dependent on the weight percentage of sulfuric acid. As the particle evaporates, the particle temperature decreases due to release of latent heat.

$T_m(x)$ depends on the wall temperature of the inlet. To estimate this, a finite difference energy balance model was developed to compute, concurrently, the wall temperature and $T_m(x)$ as air flows through the tube. The model was tested against measurements with an instrumented inlet in a laboratory cold chamber and on several balloon flights. Vertical profiles of measured and modeled temperatures, at the tip of the inlet exposed to the ambient air and at the inlet midpoint, 11 cm along the inlet, are shown in Figure 1 for a balloon flight on 4 November 2011, along with the modeled $T_m(x)$ at the inlet midpoint. The measured and modeled temperatures are in reasonable agreement except for the inlet tip at altitudes above 25 km, pressures below 25 hPa. At these low pressures convective cooling is significantly reduced and conduction along the tube dominates the temperature. To apply these results to regular OPC measurements which do not measure inlet temperatures, a relationship between ambient temperature and modeled $T_m(x)$ is calculated for the cases with inlet temperature measurements to check the model. For each altitude, $\Delta T_m(x, z) = T_m(x, z) - T_\infty(z)$ is calculated for each inlet temperature measurement. The result, $<\Delta T_m(x, z)>$, is then used to estimate $T_m(x)$ from $T_m(x, z) = T_\infty(z) + <\Delta T_m(x, z)>$. These $T_m(x, z)$ temperatures are then used to estimate evaporation of droplets in the inlet for any OPC measurement as a function of altitude. A detailed description of the inlet temperature model and its comparison with tests is given in *Kovilakam* [2012].

With an expression for $T_m(x, z)$, equivalent to T_∞ in equation (1), particle evaporation can be calculated from equation (1). Vapor pressure of H_2O over a sulfuric acid particle (p_s) is calculated using the thermodynamic model developed by *Clegg et al.* [1998]. As the particle evaporates, the weight percentage of water in the particle is reduced while the weight percentage of sulfuric acid (w_s) is increased. For $w_s > 0.8$, the expression given by *Gmitro and Vermeulen* [1964] is used to calculate p_s. For $w_s < 0.8$, the expression given by *Clegg et al.* [1998] is used. The density of a sulfuric acid particle is calculated using the method given in *Luo et al.* [1996]. The surface tension between the particle and the air is calculated from the binary sulfuric acid solution surface tension [*Tabazadeh et al.*, 2000]. A temperature-dependent weight percentage [*Steele and*

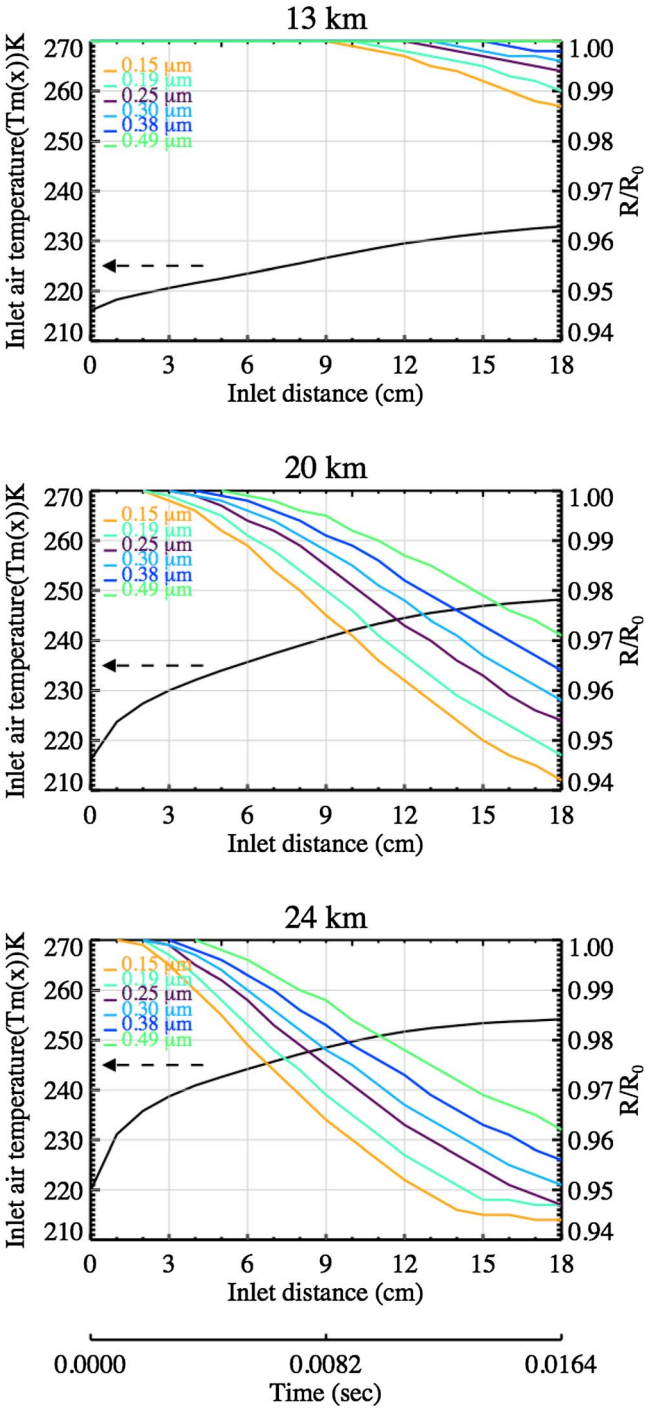

Figure 2. The ratio of evaporated to ambient particle radius (R/R_0) for different radii (scale on right) as a function of inlet length at altitudes of 13, 20, and 24 km. The mean inlet air temperature is shown in black, scale on the left.

Hamill, 1981] is used to calculate the weight percentage of sulfuric acid (w_s). The particle evaporation in the inlet results in a change of weight percentage of sulfuric acid which leads to changes in the saturation vapor pressures and latent heat. The decrease in radius caused by evaporation also leads to changes in the modified diffusion coefficient and the modified thermal conductivity. For any aerosol profile the impact of evaporation is calculated using the ambient air temperature and the expression for $\Delta T_m(x, z)$ to estimate $T_m(x, z)$. With $T_m(x, z)$ equation (3) is solved numerically for T_a and equation (1) integrated for r_a for each time step as the particle transits the inlet.

Figure 2 shows the results of a calculation, as the percentage change in particle radius due to evaporation, at 13, 20, and 24 km for a flight on 10 June 1996. $T_m(x)$ through the inlet as a function of time is also shown. For a 0.15 μm particle, a maximum of about 6% decrease in radius due to evaporation of water from an H_2SO_4-H_2O particle occurs at 20 and 24 km. The rate of size change due to evaporation decreases as the size of the particle increases since the water evaporated constitutes a smaller portion of the volume. Particle evaporation decreases below 20 km because the inlet temperature being lower (≤230 K at 13 km) at lower altitudes. This modeling study of evaporation in the OPC inlet indicates that the ambient particles measured could be up to 6% larger than the OPC size thresholds, with the differences decreasing as size increases. Although these differences are smaller than the precision claimed for the OPC sizes [*Deshler et al.*, 2003a], they are systematic and thus will be incorporated into the corrected size measurements from the OPC.

2.1.2. Anisokineticity

Aerosol sampling is isokinetic when the gas streamlines entering an inlet are not deformed by the inlet. This occurs for an inlet aligned parallel to the gas streamlines with the gas entering the inlet at a velocity equal to the free-stream velocity approaching the inlet. The inlet in the OPC is vertical and thus aligned parallel to the gas streamlines as the instrument ascends. The free-stream velocity, U_0, is the ascent rate of the balloon, nominally 5 m s^{-1}, while inlet air velocity, U, is approximately 11 m s^{-1}, for a flow rate of 10 L min^{-1} and an inlet of radius 4 mm on an OPC_{40}. Thus, the sampling is superisokinetic

($U > U_0$) which will undercount larger particles. Particles with high inertia cannot follow the converging streamlines to enter the inlet.

For a sampling inlet, the ratio of measured concentration, C, to ambient concentration, C_0, is given by [*Belyaev and Levin*, 1974]

$$A = \frac{C}{C_0} = 1 + \left[\frac{U_0}{U} - 1\right]\left[1 - \frac{1}{1 + \left(2 + 0.62\frac{U}{U_0}\right)\mathrm{Stk}}\right], \tag{4}$$

where Stk is the Stokes number. The ratio of concentrations $\frac{C}{C_0}$ is the aspiration efficiency, which can be less than one for superisokinetic sampling depending on particle size. The particle loss in the OPC is not large. For a 0.50 μm particle the maximum loss is about 6–10% above 25 km, yet 0.5 μm particles are seldom found above 20 km. For particles < 0.5 μm the aspiration efficiency indicates a particle loss of about 2% above 20 km. While the data can be corrected for anisokineticity using equation (4), the impact is negligible for most measurements and swamped by other counting uncertainties.

2.1.3. Counting Efficiency

For the UW OPC, particle detection is accomplished using photomultiplier tubes (PMTs). The response to a particle in the beam is a voltage pulse, which is analyzed for maximum pulse height and compared with the preset voltage boundaries for each size channel. The pulse generated by a particle in the beam is counted in every channel with a voltage threshold below the pulse generated by the particle. Thus, the measurement is a cumulative size distribution, with the counts in each channel representing all particles with size greater than the particle size threshold for that channel. The particle counts in each channel are reported every 10 s sampling interval and then cleared. For both the OPC_{25} and OPC_{40}, there are two PMTs focused on the air sample stream. A particle count in any channel is accepted only when coincident pulses from both PMTs are received by the pulse height analyzer. This is done to eliminate the influence of cosmic rays at low pressures and to reduce background noise. The gain of each PMT is adjusted independently to provide a pulse height, which matches the expected pulse height for the polystyrene latex (PSL) calibration aerosol. For analysis, each channel boundary is converted to size using the theoretical counter response function for the instrument assuming Mie scattering [*Hofmann et al*., 1975; *Deshler et al*., 2003a].

Ideally, the pulse height distribution for monodispersed aerosol is a narrow Gaussian curve which peaks at the size of the aerosol, with half of the pulses below the threshold and half above, since pulses from the monodispersed aerosol will be randomly distributed around the peak. The size threshold of any OPC channel is set for the peak in the Gaussian curve for particles at that channel boundary. The counting efficiency of a particle counter is the ratio of the number counted to the ambient number. This ratio describes the percentage of particles counted at or above a particular size. Typically a 50% counting efficiency is used, since that makes the calibration of a pulse height detector independent of the shape of the pulse height distribution [*Xu*, 2001]. When coincident counting is used with two PMTs, and if each PMT is calibrated separately, the resulting overall counting efficiency of the instrument is the product of the pulse distributions from the two phototubes. Thus, for PMTs individually calibrated for a counting efficiency of 50%, the overall counting efficiency of the two PMTs will be the product of the two counting efficiencies, or 25% for randomly distributed pulses.

The two-channel OPC_{25}, developed in the late 1960s and early 1970s, prior to the advent of digital pulse height analysis, employed a calibration system which compared counts in the second channel to counts in the first, using particles at the bin boundary of the second channel for calibration. With this system the gains on each PMT were adjusted to a counting efficiency of approximately 70% leading to an overall counting efficiency of 50% for particles at the bin boundary of the second channel. Since there is a fixed relationship between all channels in a gain stage, defined by the counter response function, the counting efficiency of all other channels will be similar.

In 1989, the design of the Wyoming OPC was modified to produce an unambiguous counter response function from 0.15 to 10.0 μm and to reduce the minimum measurable concentration. The primary interest was in situ measurements of polar stratospheric clouds [*Hofmann and Deshler*, 1991]. A secondary benefit was higher-resolution size measurements following the Pinatubo eruption when the size range was

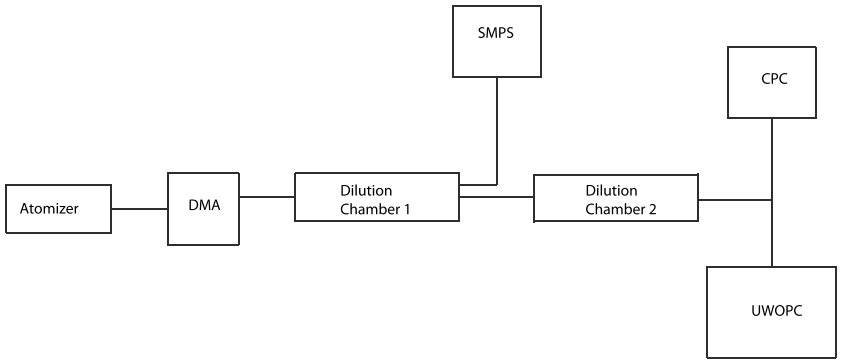

Figure 3. Schematic of lab setup for counting efficiency test. The instruments used are differential mobility analyzer (DMA), scanning mobility particle sizer (SMPS), condensation particle counter (CPC), and University of Wyoming optical particle counter (UWOPC).

reduced to 0.15–2.0 μm [*Deshler et al*., 1993]. To minimize the Mie resonances near 0.5 μm, the forward scattering angle of the photodetectors was increased from 25° to 40° (OPC_{40}). This provided an unambiguous counter response for particles between 0.3 and 1.0 μm, the difficult region for the OPC_{25}. For the OPC_{40} three gain stages were required to span the size range, and this required a new calibration system, which took advantage of the pulse height analysis systems available at that time. Thus, for the first time, the pulse height distribution from a single PMT and gain stage was used for calibration. Instrument calibration then required adjusting feedback potentiometers, for each PMT on each gain stage, until the peak in the measured pulse height distribution matched the theoretical pulse expected for the calibration aerosol, based on the counter response function. This method implies a 50% counting efficiency for each PMT at every channel of every gain stage. This change, in OPC design and calibration system, was coincident with a change of personnel doing the calibrations and using the data. The result of these simultaneous changes was that the impact of the calibration system change on the overall OPC counting efficiency, as the product of the counting efficiency of each PMT, was not realized until recently.

To confirm this analysis, the W. M. Keck aerosol laboratory at the university was used to test the overall instrument counting efficiencies, using monodispersed ammonium sulfate particles, for an OPC_{40} and OPC_{25}. Ammonium sulfate has a higher refractive index (1.52) than sulfuric acid-water (1.45), at the OPC wavelength (500 nm), but this affects the counter response minimally, and ammonium sulfate is much easier to handle than sulfuric acid-water particles. A schematic of the laboratory setup is shown in Figure 3. Ammonium sulfate salt solution is atomized, dried, and charge neutralized, before being size selected with a differential mobility analyzer (DMA). The particles exiting the DMA are then diluted with filtered air and sampled with a scanning mobility particle sizer (SMPS), which measures the test size distribution. A second dilution chamber is used to dilute the concentration further to produce a particle concentration that resembles that of stratospheric aerosol ($<10\,cm^{-3}$). A condensation particle counter (CPC) is used as the reference concentration instrument for testing the counting efficiency. Both the CPC and OPC are connected to the second dilution chamber. For each particle size, the counting efficiency of the OPC can be written as the ratio of N_m, the measured OPC concentration, and N_t, the concentration measured by the CPC.

The threshold radii of a midlatitude OPC_{40} are 0.15, 0.19, 0.25, 0.30, 0.38, 0.49, 0.62, 0.78, 1.08, 1.25, 1.58, and 2.0 μm. For the counting efficiency tests, only the smallest three channels could be tested, but these represent two gain stages: 0.15 and 0.25 μm on the high gain board and 0.19 μm on the mid gain board. The DMA has an upper limit of 0.35 μm but could not generate sufficient concentrations of ammonium sulfate particles >0.25 μm. Although the sizing sensitivity of the OPC_{40} to larger particles has been checked with PSL particles [*Deshler et al*., 2003a, 2003b] and is calibrated with PSL, it is not possible to limit a CPC measurement to detection of only PSL particles and prohibit detection of all smaller particles that derive from the water in which the PSL are suspended and aspirated. Since the concentration of the

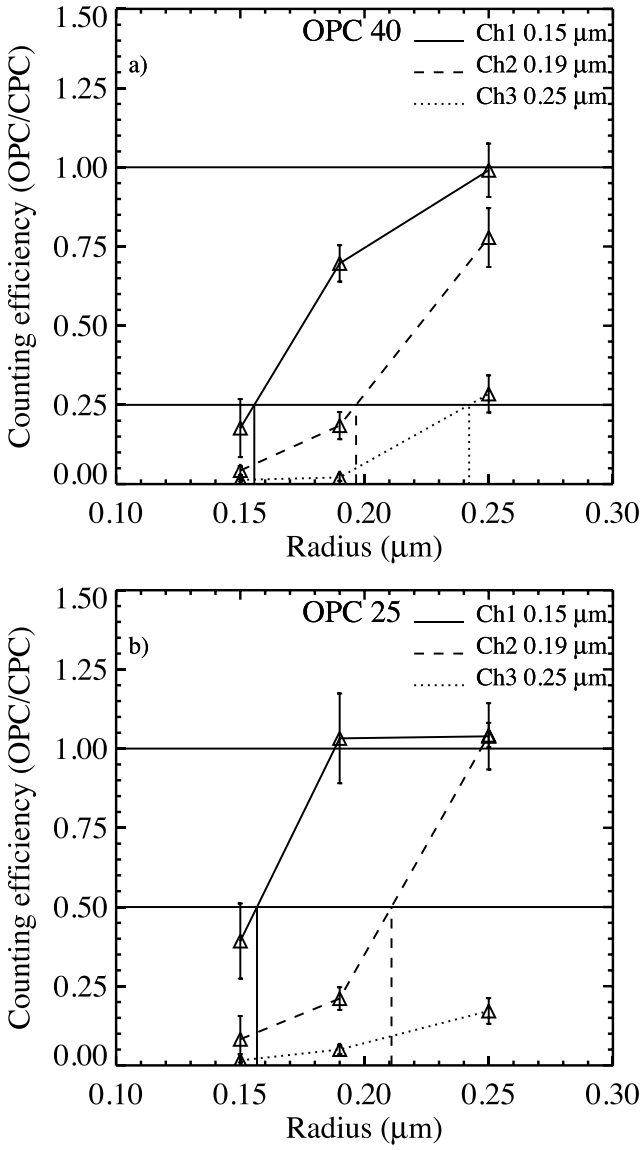

Figure 4. Average OPC counting efficiency for 0.15, 0.19, and 0.25 μm particles as a function of radii of ammonium sulfate particles tested for (a) OPC_{40} and (b) OPC_{25}. Error bars represent one standard deviation of the four measurements on each instrument. Vertical lines show the radii for which the counting efficiency is the expected 25% for the OPC_{40} and 50% for the OPC_{25}.

small particles from contaminants in the water would overwhelm the low concentrations of PSL required, there is no concentration reference for tests with particles > 0.25 μm.

The results of four laboratory tests using ammonium sulfate are shown in Figure 4a for an OPC_{40} and Figure 4b for an OPC_{25}. The counting efficiencies for the OPC_{40} to ammonium sulfate particles of radii of 0.15, 0.19, and 0.25 μm are 18, 19, and 29%, respectively. These are close to the 25% expected. With a linear interpolation, 25% counting efficiencies are observed at 0.155, 0.196, and 0.243 μm, sizes well within the size precision expected for the instrument. In Figure 4b the counting efficiencies for the OPC_{25} for particles of radii of 0.15, 0.19, and 0.25 μm are 39, 21, and 17%, respectively. In this case, after linearly interpolating between the sizes, the 50% counting efficiencies are observed at 0.156 and 0.210 μm, which are close to the nominal channel boundaries. The measurements do not allow an assessment of the 50% counting efficiency for the 0.25 μm channel for an OPC_{25}.

The measured counting efficiencies from the lab tests are available only for the first three channels of the OPC_{40}; however, these measurements are consistent with the 25% counting efficiency expected, within experimental uncertainty, for the instrument. Thus, extrapolation of this counting efficiency to the larger channels is considered reasonable.

The laboratory tests support the analysis of PMT response for the OPC_{25} and OPC_{40}, indicating that the counting efficiency of an OPC_{25} is near 50% and for an OPC_{40} is near the 25% expected, based on a pulse height distribution centered at 50% for calibration of each PMT at each gain stage of the OPC_{40}. Therefore, based on the laboratory tests and counting efficiency analysis for two PMTs, a correction needs to be applied to the number concentrations measured to appropriately increase the concentration for OPC_{40} measurements at sizes which have less than the ideal counting efficiency of 50% for particle counters [*Xu*, 2001]. This correction, however, is not as simple as increasing the number concentration in all channels by a factor of 2, since the counting efficiency also depends on the shape of the particle size distribution. For example, at the extreme, if adjacent size channels have equal or nearly equal concentrations, the counting efficiency of the smaller channel would be near one because all particles are much greater than that channel's size threshold and would be counted. Thus, applying an additional correction would artificially inflate the measured number

concentration in the smaller channel. For this reason, the slope, fdn, calculated directly from measurements of the cumulative concentration size distribution is used, along with a linear empirical formula, to relate the laboratory measured counting efficiency, $CE_M = 0.25$, to the real counting efficiency, CE_N, given by

$$CE_N(i) = 0.5 + (CE_M - 0.5)A_i, \quad (i = \text{channel number}; \ i = 1, 2, \ldots, 12)$$

$$A_i = \begin{cases} \text{fdn}(i)/\text{fdn}_{\text{ref}} & \text{fdn}(i) < \text{fdn}_{\text{ref}} \\ 1 & \text{fdn}(i) > \text{fdn}_{\text{ref}} \end{cases} \quad \text{and} \tag{5}$$

$$\text{fdn}(i) = \frac{\ln\left(N_i / N_{i+1}\right)}{\ln\left(\frac{r_{i+1}}{r_i}\right)}. \tag{6}$$

The number concentration correction factor, C_f, is then given by

$$c_f(i) = 0.5 / C_{E_N} \quad \text{and} N_C(i) = C_f(i) \times N(i), \tag{7}$$

where $N_C(i)$ is the corrected concentration and $N(i)$ is the measured concentration. fdn is the slope of the cumulative size distribution, whereas fdn_{ref} is a reference value of fdn to determine if a full correction should be applied. If the slope fdn(i) is greater than fdn_{ref}, then a full counting efficiency correction is applied for that channel. In practice, fdn_{ref} is used to calculate a reference comparison concentration for each subsequent size in a distribution. If the measured concentration at the next size is less than the reference concentration, then a full correction is applied; if greater than the reference concentration, then a scaled partial correction is applied.

Term $A(i)$ in equation (5) varies from 0 to 1. The minimum value of 0 occurs when two adjacent channels have the same concentration and leads to $CE_N(i) = 0.5$, and thus, $C_f(i) = 1$. If $A(i)$ is 1 and $CE_M = 0.25$, then $CE_N(i) = 0.25$ and $C_f(i) = 2$. The corrected concentration ($N_C(i)$) of that particular channel is then $2 \times N(i)$. This method breaks down for the smallest OPC size. There is no comparator lower channel. Measurements of CN were tried, but this creates a large denominator due to the differences in size between the OPC at 0.15 μm and the assumed size for CN 0.01 μm. That left using the value of fdn(i) for the second OPC size to be applied to the number concentrations in the first OPC size channel.

The choice of fdn_{ref} is somewhat arbitrary, and a range from 4 to 10 was explored. The choice determines the fraction of measurements to which less than a full correction of 2 is applied. Considering that there are few independent measurements of stratospheric aerosol for comparison with the OPC_{40} measurements, the SAGE II comparisons, discussed above and shown below, are an important consideration in the choice of fdn_{ref}. Based on the shape of the size distributions in the two periods it is expected that the nonvolcanic, low aerosol loading period would require more correction since these distributions are generally steeper.

The data from 1990 to 2005 were analyzed for probability distributions of fdn(i) and thus of $Cf(i)$ for fdn_{ref} varying from 4 to 10. The value of Cf, and the fraction of measurements for which Cf is less than a full correction, $C_f = 2$, vary as the value of fdn_{ref} varies, yet the choice of fdn_{ref} is somewhat arbitrary. The approach selected was to correct the OPC number concentrations for a range of fdn_{ref} and to compare the resulting calculated extinction profiles with SAGE II data at 1.02 and 0.525 μm for both the volcanic and nonvolcanic period. The range of calculated extinctions resulting from the range of fdn_{ref} used (4–10) is larger during the nonvolcanic period than during the volcanic period; thus, the selection of fdn_{ref} is more heavily weighted to the nonvolcanic measurements, since the range of the effect is larger during the nonvolcanic period. Balancing all the comparisons against the SAGE II-measured extinctions resulted in a selection of $\text{fdn}_{\text{ref}} = 6$. For the average ratios of adjacent OPC particle size, $\frac{r_i}{r_{i+1}} \sim 0.8$, $\text{fdn}_{\text{ref}} = 6$ occurs when particle concentration decreases by ~75% between adjacent sizes. This selection results in approximately 40% of the volcanic measurements experiencing a full correction, whereas over half of the nonvolcanic measurements have a full correction applied. As will be shown, the variation of fdn_{ref} does not affect the comparisons greatly.

2.1.4. Summary of Corrections Applied to the OPC Measurements

Corrections for evaporation of the particles in the inlet, anisokineticity, and counting efficiency are now incorporated into the measurements, and new size distributions are estimated for the OPC_{40} measurements. Figures 5a and 5b show differential and cumulative distributions of concentration at 20 km, for example,

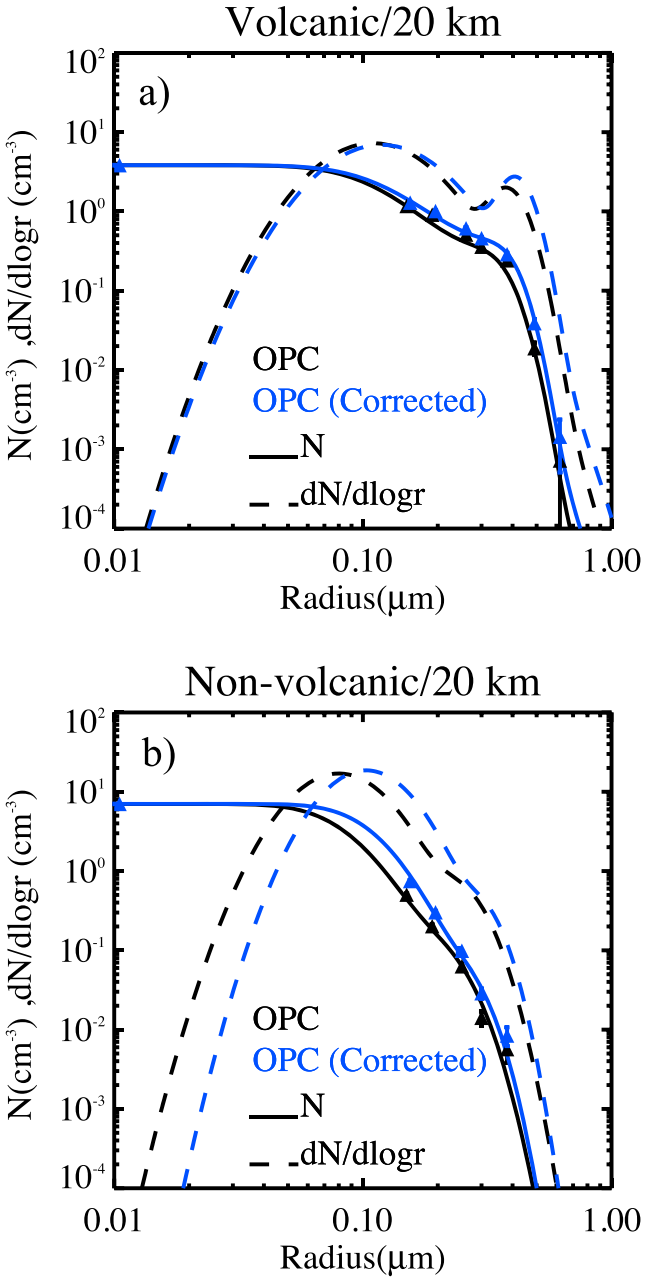

Figure 5. Bimodal lognormal differential distributions (dashed lines) and cumulative distributions (solid lines) of concentration for a (a) volcanic (19940308 implies 08 March 1994) and (b) nonvolcanic (20000412 implies 12 April 2000) measurement at 20 km. Measurements are shown as triangles. Black lines represent OPC measurements with no correction applied, while blue lines represent OPC measurement with all corrections (evaporation + anisokineticity + counting efficiency correction). Uncertainties from Poisson counting statistics are shown on the concentration measurements but are not larger than the data symbols until low concentrations are reached. Anisokineticity and counting efficiency change the number concentration, while evaporation affects the sizes. This latter change can only really be seen in Figure 5b at 0.15 μm, which is the size most affected.

volcanic (19940308 implies 08 March 1994) and nonvolcanic (20000412 implies 12 April 2000) measurements. The evaporation and isokinetic correction have little effect on either size distribution and are not observable in the figure. The counting efficiency correction is the dominant effect especially for the first few channels of the nonvolcanic case. In particular, the effect on the size distribution can be clearly seen, where the peak height of the smaller particle size mode becomes higher and narrower while being shifted toward a larger size. These changes in size distribution parameters will increase the derived aerosol moments such as extinction and surface area.

3. Comparisons of OPC With SAGE II and HALOE Extinction Measurements

SAGE II, launched on the Earth Radiation Budget Satellite on 5 October 1984, was designed to monitor the global distribution of stratospheric aerosols, ozone, nitrogen dioxide, and water vapor [*Mauldin et al.*, 1985], using measurements of solar radiation that passes through the limb of the Earth's atmosphere as the satellite rises and sets over the horizon. The intensity of solar radiation is determined with a seven-channel Sun-scanning spectrometer. The transmission data from these seven channels are then used to derive particulate extinction and concentrations of ozone, nitrogen dioxide, and water vapor [*Chu et al.*, 1989; *Wang et al.*, 1994; *Damadeo et al.*, 2013]. Measurements are taken from a tangent height of 150 km, where there is no attenuation, down to the point where the Sun is obscured by clouds or terrain, with a vertical resolution of 0.5 km. The orbital configuration allows spatial coverage of solar occultation between 80°N and 80°S, with approximately 15 sunrise and 15 sunset measurements in 24 h. SAGE II aerosol extinction measurements are made at 1.02, 0.525, 0.452, and 0.386 μm wavelengths. Aerosol SAD is calculated using an empirical parameterization, which was based on principal component analysis, but is now modified increasing the range of possible SAD from SAGE II [*Thomason et al.*, 2008; *Damadeo et al.*, 2013]. The SAGE II mission ended in 2005.

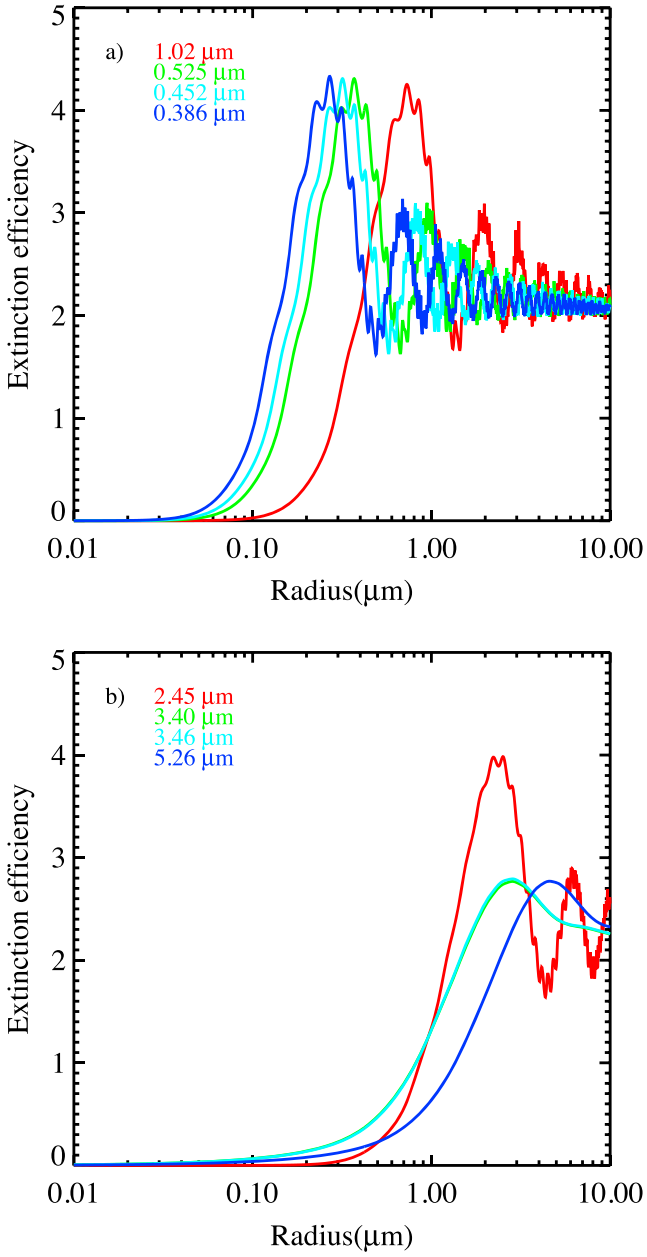

Figure 6. Extinction efficiencies as a function of particle radius (a) at SAGE II wavelengths of 1.02, 0.525, 0.452, and 0.386 μm, using refractive indices of 1.45, 1.47, 1.47, and 1.48, respectively, and (b) at HALOE wavelengths of 2.45, 3.40, 3.46, and 5.26 μm using refractive indices of 1.34, 1.36 + *i* 0.16, 1.37 + *i* 0.16, and 1.34 + *i* 0.14, respectively.

The SAGE II version 6.2 and 7.0 data products are used in this study. In version 7.0, 1.02 μm aerosol extinction is consistent with the previous version 6.2; however, there are large changes in extinction between 20 and 30 km (20–35% less compared to version 7.0) in 0.525 μm extinction due to spectroscopic changes in version 7.0 [*Damadeo et al.*, 2013]. Aerosol SAD is also updated in version 7.0 with a method, which increases the SAGE II SAD by about 50% during the nonvolcanic period [*Thomason et al.*, 2008].

HALOE, launched on the upper atmosphere research satellite, reported science observations from 11 October 1991 to 21 November 2005. HALOE also uses solar occultation to measure vertical profiles of seven gases (hydrochloric acid, hydrogen fluoride, methane, nitric oxide, nitrogen dioxide, water vapor, and ozone), temperature, and aerosol extinction at four wavelengths (2.45, 3.40, 3.46, and 5.26 μm) [*Russell et al.*, 1993]. Latitudinal coverage is from 80°S to 80°N, and the altitude range extends from about 15 km to 60–130 km depending on the species. The HALOE version 19 data are used in this study. HALOE SAD has been calculated from unimodal lognormal aerosol size distributions, retrieved from the extinction measurements [*Hervig et al.*, 1998], but this is not a standard HALOE data product and is distributed without caveat.

For comparison of SAGE II measurements with balloon-borne in situ OPC_{40} measurements from Laramie, Wyoming, (41°N, 105°W), coincident measurements are identified using a maximum separation of 168 h, a 6° latitude band centered at Laramie, and longitudes between 90°W and 120°W. The wide longitude band leads to multiple coincidences for a single balloon flight. For the period 1991–1996, following the Pinatubo volcanic eruption, there are 34 OPC profiles and 80 corresponding SAGE II profiles. These profiles will be referred to as volcanic. In the subsequent nonvolcanic or background period, 1997–2005, there are 12 OPC profiles and 22 SAGE II profiles. Applying the same coincidence criteria to HALOE and OPC_{40} measurements resulted in 31 OPC profiles and 75 corresponding HALOE profiles for the volcanic period and 5 OPC profiles and 14 corresponding HALOE profiles during the nonvolcanic period. The fewer number of nonvolcanic profiles reflects a reduction in the in situ sampling frequency.

Mount Pinatubo in the Philippines at 15°N erupted on 15 June 1991. Measurements from a number of sources showed that it took 5–6 years for the volcanic stratospheric aerosol levels to decay to pre-Pinatubo

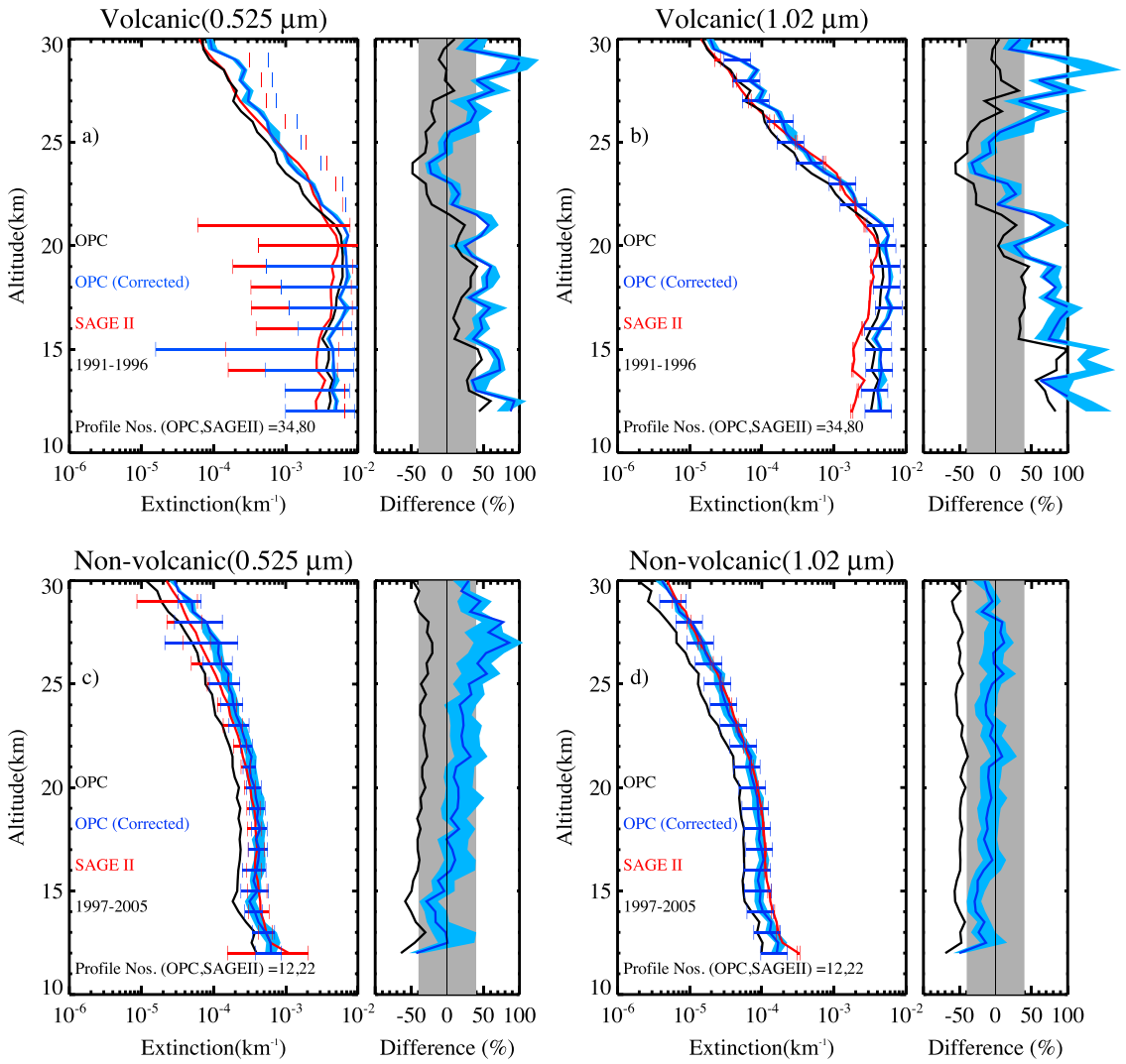

Figure 7. Average extinction profiles of OPC (black and blue) and SAGE II version 7.0 (red) at wavelengths of 1.02 and 0.525 μm, along with mean percentage differences (OPC-SAGEII)/SAGEII, for (a and b) the volcanic period, 1991–1996, and (c and d) the nonvolcanic period, 1997–2005. Blue shading represents the range of fdn_{ref}, bounding from $fdn_{ref} = 4$ to $fdn_{ref} = 10$. Grey shading represents the OPC precision range. Black represents the OPC extinction without any correction, blue after correcting for evaporation, anisokineticity, and counting efficiency. The error bars for both OPC and SAGE II extinction at 0.525 μm show one standard deviation of the measurements, whereas at 1.02 μm extinction, the error bars represent the ±40% precision of OPC extinction and the SAGE II measurement uncertainty. The total number of comparisons for each period is shown at the bottom of the extinction profiles.

background levels [*Jäger*, 2005; *Deshler et al.*, 2006; *Wilson et al.*, 2008]. The volcanic period thus represents Pinatubo aerosol and its decay.

3.1. Aerosol Extinction Comparisons

The primary aerosol measurements of SAGE II and HALOE are extinction, and these extinction measurements are used to derive SAD. Thus, the natural starting point for comparisons with SAGE II and HALOE is through extinction. The primary aerosol measurement from the OPCs is particle size and concentration, from which size distributions are derived, and aerosol extinction calculated using

$$\beta_\lambda = \int_0^\infty \pi r^2 Q(r,\lambda,m) \frac{dn}{dr} dr, \tag{8}$$

where r is the radius of the particle, $Q(r,\lambda,m)$ the extinction efficiency, λ wavelength of light, m refractive index, and $\frac{dn}{dr}$ the aerosol size distribution fitted to the OPC measurements.

To complete the extinction calculations from the OPC measurements requires the extinction efficiency, $Q(r, \lambda, m)$, which is a function of particle composition, through the refractive index, and shape (not indicated). Stratospheric aerosol are primarily small liquid, thus spherical, droplets of sulfuric acid and water [*Rosen*, 1971], with the composition typically given in weight percentage (wt %) of H_2SO_4. *Steele and Hamill* [1981] report a relationship between the temperature and weight percentage of sulfuric acid. By fitting cubic splines to temperature-dependent weight percentages, the weight percentage of sulfuric acid can be approximated using the measured temperature. With the weight percentage of sulfuric acid calculated using Steele and Hamill, refractive indices can be estimated from *Palmer and Williams* [1975] data at 300 K by interpolation for any acid concentration and wavelength. Finally the real part of the refractive index is corrected to the measured stratospheric temperatures by applying the Lorentz-Lorenz formula, with the density of sulfuric acid, ρ, calculated from *Luo et al.* [1996]:

$$m(T) = \left(\frac{2A\rho(T)+1}{1-A\rho(T)}\right)^{1/2}, \quad \text{where } A = \frac{m^2(300)-1}{[m^2(300)+2]\,\rho(300)}. \tag{9}$$

For SAGE II wavelengths the refractive index has only a real (scattering) component, whereas for HALOE there is also an imaginary (absorbing) component for wavelengths $> 2.5\,\mu m$. As for SAGE II, the refractive indices for HALOE are from *Palmer and Williams* [1975]. The refractive indices are checked against *Niedziela et al.* [1998] and found to be in good agreement. Given the refractive index, Mie theory for spherical particles is used to calculate extinction efficiency as a function of particle radius for SAGE II and HALOE and shown in Figure 6.

Typically stratospheric aerosol size distributions can be approximated using lognormal distributions [*Pueschel et al.*, 1992, 1994; *Deshler et al.*, 2003a]; thus, dn/dr is given by

$$\frac{dn}{dr} = \sum_i \frac{N_i}{r\sqrt{2\pi}\ln\sigma_i} \exp\left(\frac{-\ln^2\left(\frac{r}{r_{mi}}\right)}{2\ln^2\sigma_i}\right), \tag{10}$$

where i represents the mode number (1 or 2), N_i is the total number concentration per mode, r_{mi} is the median radius per mode, and σ_i is the distribution width per mode. The size distribution parameters in equation (10) are derived from the OPC measurements by fitting the measurements with both unimodal and, if there are enough sizes measured, bimodal lognormal distributions. The final size distribution used is the one which minimizes the difference between the fit and the measurements [*Deshler et al.*, 2003a]. These size distribution parameters for the history of OPC measurements are available at http://www-das.uwyo.edu/~deshler/Data/Aer_Meas_Wy_read_me.htm. Extinction is calculated using equations 8–10 at each altitude interval of 0.5 km, for each SAGE II and HALOE wavelength.

Extinction measurements from SAGE II are more reliable at the two longer wavelengths (1.02 and 0.525 μm) than at the shorter wavelengths because of molecular Rayleigh scattering [*Thomason et al.*, 2008]. Thus, only measurements taken at 1.02 and 0.525 μm are compared here. The extinctions at 1.02 and 0.525 μm have only a small bias of about 10–20% for SAGE II version 6.2 [*SPARC*, 2006]. The biases were decreased in the version 7.0 SAGE II data [*Thomason et al.*, 2008]. Figure 7 shows averaged vertical profiles of the OPC and SAGE II version 7.0 extinctions for the volcanic and nonvolcanic periods, and the difference of the mean profiles, (OPC-SAGEII)/SAGEII. The error bars for both OPC and SAGE II at 0.525 μm extinction represent one standard deviation of the measurements, showing the geophysical variability over the period (Figures 7a and 7c), while at 1.02 μm extinction the error bars show the measurement uncertainties of OPC and SAGE II (Figures 7b and 7d). The shaded area of the corrected OPC profiles, and of the differences using the corrected OPC data, show the variation of results with an fdn_{ref} range of 4–10, indicating the small dependence on the choice of fdn_{ref}.

For the uncorrected OPC measurements during the volcanic period (Figures 7a and 7b), the OPC extinction estimates are somewhat high below 22 km, somewhat low from 22 to 27 km, and then in good agreement above 27 km. During the nonvolcanic period (Figures 7c and 7d), the uncorrected OPC extinctions are about a factor of 2 lower than the SAGE II extinctions throughout the profile. For the corrected OPC extinctions, during the volcanic period, the overestimation of SAGE II extinction below 22 km is increased by 10–20%, while the agreement between 22 and 27 km is improved and then worsens above 27 km. During the nonvolcanic period the corrected OPC extinctions are in significantly better agreement with the SAGE II extinctions

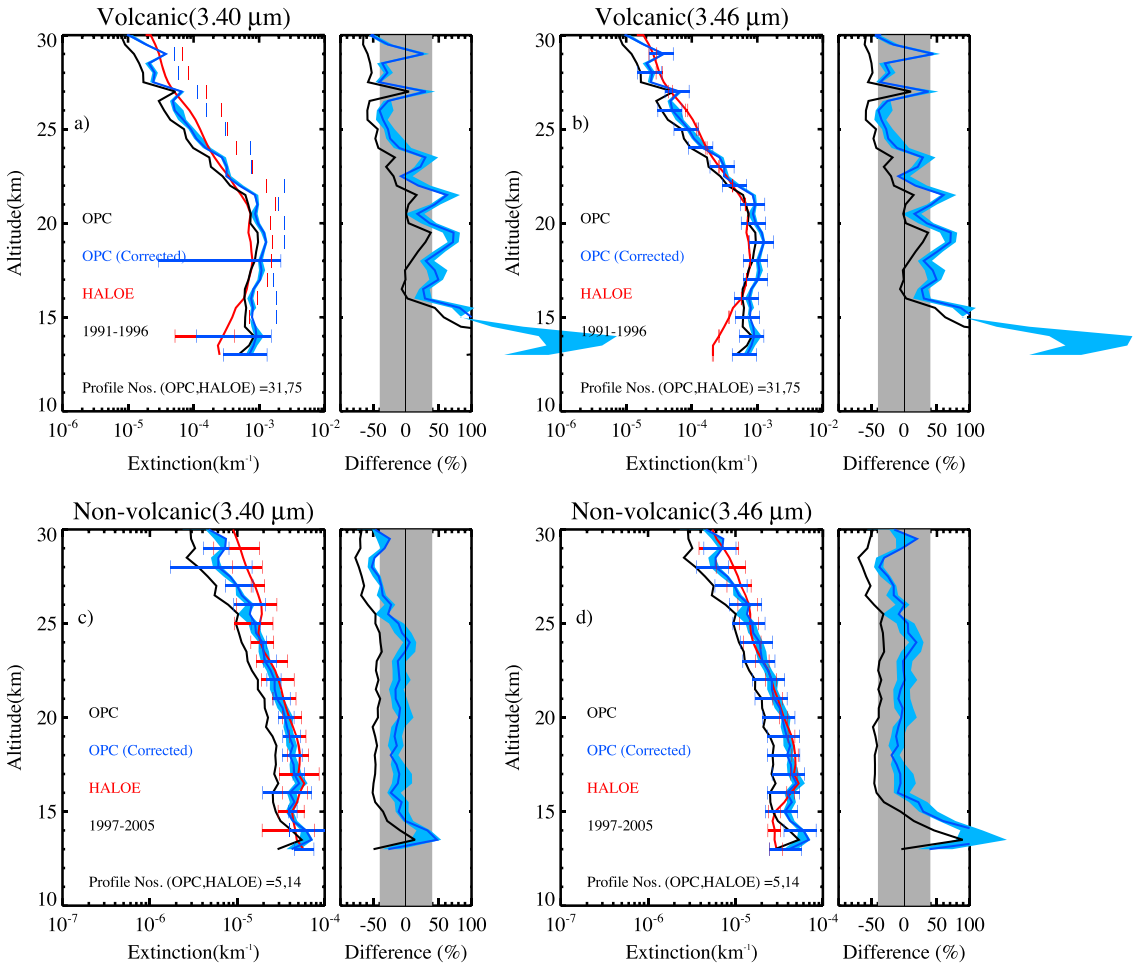

Figure 8. As Figure 7 but for HALOE measurements.

throughout the profile, and in all cases within the ± 40% precision of the corrected OPC extinctions, except above 26 km for 0.525 μm. Unfortunately, the corrections degrade the comparison for the volcanic period, particularly at 1.02 μm where the difference exceeds ± 40% at altitudes below 20 km and above 26 km. The results are better at 0.525 μm. The source of the difference at 1.02 μm is not understood; it would imply a sensitivity of the OPC to larger aerosol that are not contributing to the SAGE II measurements. Perhaps the second mode of the size distributions in this region are is a little too wide. This was not investigated further.

A similar comparison is made with HALOE extinction measurements at 3.40 and 3.46 μm. Extinction measurements at 2.45 and 5.26 μm are not recommended for scientific purposes during the low aerosol loading period after 1996 [*Thomason*, 2012]. According to *Thomason* [2012], 3.46 μm extinction is of good quality above 19 km and 3.40 μm extinction is biased by about +10% throughout the stratosphere. Figure 8 shows vertical profiles of the OPC and HALOE extinction for the volcanic and nonvolcanic periods. The error bars for both OPC and HALOE at 3.40 μm extinction represent one standard deviation of the measurements, showing the geophysical variability over the period (Figures 8a and 8c), while at 3.46 μm extinction the error bars show the measurement uncertainties of OPC and HALOE (Figures 8b and 8d).

For the uncorrected OPC measurements during the volcanic period, the agreement is reasonable at 17–22 km (Figures 8a and 8b). Below 17 km the OPC overestimates HALOE while underestimating HALOE extinction above 22 km. During the nonvolcanic period, the uncorrected OPC extinctions are a factor of 2 below HALOE extinctions through most of the profile increasing to a factor of 4 above 25 km (Figures 8c and 8d). For the corrected OPC extinctions during the volcanic period, the agreement in regions of previous over (under) estimation worsen (improve), while the region of previous agreement changes to an overestimation of 25–50%. For the nonvolcanic period the corrected OPC extinctions increase by about a factor of 2 below

25 km bring them into significantly better agreement with the HALOE extinctions throughout the profile; however, OPC extinctions are still low by 50% or more above 25 km. Throughout much of both volcanic and nonvolcanic profiles the HALOE extinction falls within the ±40% precision of the OPC calculated extinction.

3.2. Surface Area Density Comparisons

OPC-derived SAD estimates (SAD_{OPC}) can be calculated directly from the size distribution measurements,

$$SAD_{OPC} = \int_0^\infty 4\pi r^2 \frac{dn}{dr} dr. \tag{11}$$

Surface area from SAGE II has in the past been retrieved using a technique called principal component analysis (PCA). In the PCA analysis of *Thomason et al*. [1997], coefficients were selected such that the retrieval emphasizes the longer wavelengths (1.02 and 0.525 μm) which are believed to provide more reliable information [*SPARC*, 2006; *Thomason et al*., 2008]. For operational purposes in the SAGE II data version 6.2, this approach was used to develop a simplified expression for SAD, given by

$$SAD_{SAGE\,II} = k_{1020}\left(\frac{1854.97 + 90.137r + 66.97r^2}{1 - 0.1745r + 0.00858r^2}\right), \tag{12}$$

where r is the 0.525 to 1.02 μm aerosol extinction ratio and k_{1020} is the 1.020 μm aerosol extinction coefficient.

SAD estimated by equation (12) underestimates SAD during nonvolcanic periods [*Deshler et al*., 2003a; *SPARC*, 2006; *Reeves et al*., 2008]. The known problems with PCA analyses [*Steele et al*., 1999; *Thomason et al*., 1997; *SPARC*, 2006] led *Thomason et al*. [2008] to propose a new method (Method 1) to calculate a minimum and a maximum SAD during nonvolcanic periods. Method 1 is based on assuming that SAD arises from two monodispersed aerosol size distributions. One of these distributions is observable with SAGE II and will be referred to here as the large particle mode with radius, r_l. This distribution will lead to the minimum SAD (SAD_{min}) which can be directly derived from SAGE II extinction measurements. For the maximum SAD (SAD_{max}), the contribution of an unobservable small monodispersed aerosol mode, centered at r_s, must be added to SAD_{min}. Since extinction at visible wavelengths from these smaller particles is undetectable, or nearly so, two assumptions are made. The first is that the uncertainty in the extinction measurement at the shortest wavelength (0.525 μm) is caused by this aerosol mode. The second is that the particles have a number density of 20 cm^{-3}. In situ measurements [*Campbell and Deshler*, 2014] indicate that total aerosol number concentrations in the stratosphere are around 10 cm^{-3}, for particles greater than 0.01 μm. *Thomason et al*. [2008] choose 20 cm^{-3} to exceed this number concentration in most circumstances in the stratosphere, because of the assumption of a monodispersed aerosol distribution, and to ensure a maximum SAD.

The basis for the calculation of r_l from extinction is that there is a unique one to one relationship between the extinction ratio and particle size for particles between 0 and ~0.5 μm [*Thomason et al*., 2008, Figure 10]. Thus, the extinction ratio can be used to identify r_l which would reproduce the extinction measurements for a monodispersed aerosol distribution at r_l. Thus, for a monodispersed aerosol, SAD_{min} occurs at the radius that provides the observed extinction $k(\lambda)$, modified by measurement uncertainty $\varepsilon(\lambda)$. Therefore, aerosol extinction can be written as

$$k(\lambda) - \varepsilon(\lambda) = N_l\, Q(r_l, \lambda)\pi {r_l}^2, \tag{13}$$

where k is the aerosol extinction coefficient, ε its associated uncertainty at wavelength λ, N_l and r_l are the number concentration and radius of the monodispersed aerosol, and $Q(r_l, \lambda)$ is the extinction efficiency shown in Figure 6a, calculated at r_l. Comparing an observed 0.525 to 1.02 μm extinction ratio ($k_{525} - \varepsilon_{525}/k_{1020}$) to the theoretical 0.525 to 1.02 μm extinction efficiency ratio ($Q(r, \lambda_{525})/Q(r, \lambda_{1020})$), using the theoretical extinction efficiency curves shown in Figure 6a, gives r_l. N_l is then calculated from equation (13), and then, $SAD_{min} = 4\pi N_l r_l^2$.

To estimate SAD_{max}, consistent with SAGE II measurements, a small particle monodispersed mode is added to the mode used to calculate SAD_{min} to bring the total number concentration (N_{tot}) to 20 cm^{-3}. SAD_{max} is given by

$$SAD_{max} = \; SAD'_{min} + 4\,(N_{tot} - N_l)\pi r_s^2, \tag{14}$$

where r_s is the radius of the small particle mode. This radius is obtained from $\varepsilon(\lambda_{min}) = Q(r_s, , \lambda_{min})\pi r_s^2 \left(N_{tot} - N_l^{'}\right)$, where N'_l and SAD'_{min} are calculated using $k(\lambda)$ instead of $k(\lambda) - \varepsilon(\lambda)$ in equation (13). The

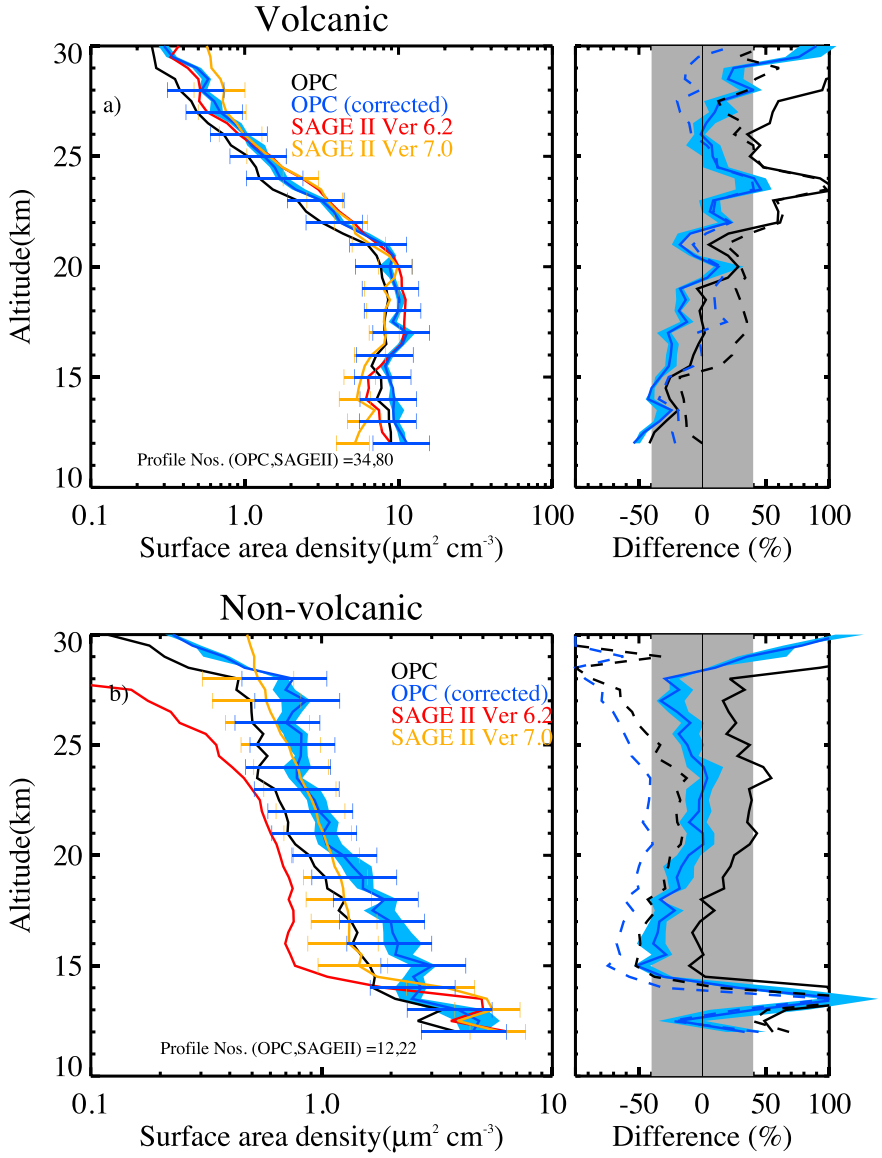

Figure 9. Average SAD profiles of OPC and SAGE II for the (a) volcanic and (b) nonvolcanic periods. $SAD_{SV6.2}$ is shown in red, $SAD_{SV7.0}$ in orange, SAD_{OPCnc} in black, and SAD_{OPCwc}, corrected for evaporation, anisokineticity, and counting efficiency, in blue. The SAD_{OPC} error bars represent ±40% precision in SAD. Vertical profiles of mean percentage differences $(SAD_{SAGEII} - SAD_{OPC})/SAD_{OPC}$ are also shown. Blue shading represents the range of fdn_{ref}, bounding from $fdn_{ref} = 4$ to $fdn_{ref} = 10$. Grey shading represents the OPC precision range. In the percentage difference calculation, both corrected (blue) and uncorrected (black) SAD_{OPC} are used. Dashed lines in the percentage difference plot represent percent difference with respect to $SAD_{SV6.2}$, while solid lines differences with $SAD_{SV7.0}$.

version 7.0 SAGE II SAD ($SAD_{SV7.0}$) is calculated as the average of SAD_{min} and SAD_{max} and is available on the SAGE II database.

Figure 9 shows mean vertical profiles of SAD from SAGE II, versions 6.2 and 7, and OPC_{40}, uncorrected (SAD_{OPCnc}) and corrected (SAD_{OPCwc}) with mean percentage differences, $(SAD_{SAGE\ II} - SAD_{OPC})/SAD_{OPC}$, for all four comparisons in each period. $SAD_{SV6.2}$ is the operational version 6.2 SAGE II SAD calculated using equation (12) and available on the SAGE II database. SAD_{max} does not work well for volcanic periods where the measured 0.525 to 1.02 μm extinction ratio is small causing ambiguity in estimations of r_f. Therefore, the new operational, $SAD_{SV7.0}$, method transitions from the *Thomason et al.* [2008] method to $SAD_{SV6.2}$ [*SPARC*, 2006] with a linear mix in between [*Damadeo et al.*, 2013]. As a result, $SAD_{SAGE\ II}$ does not

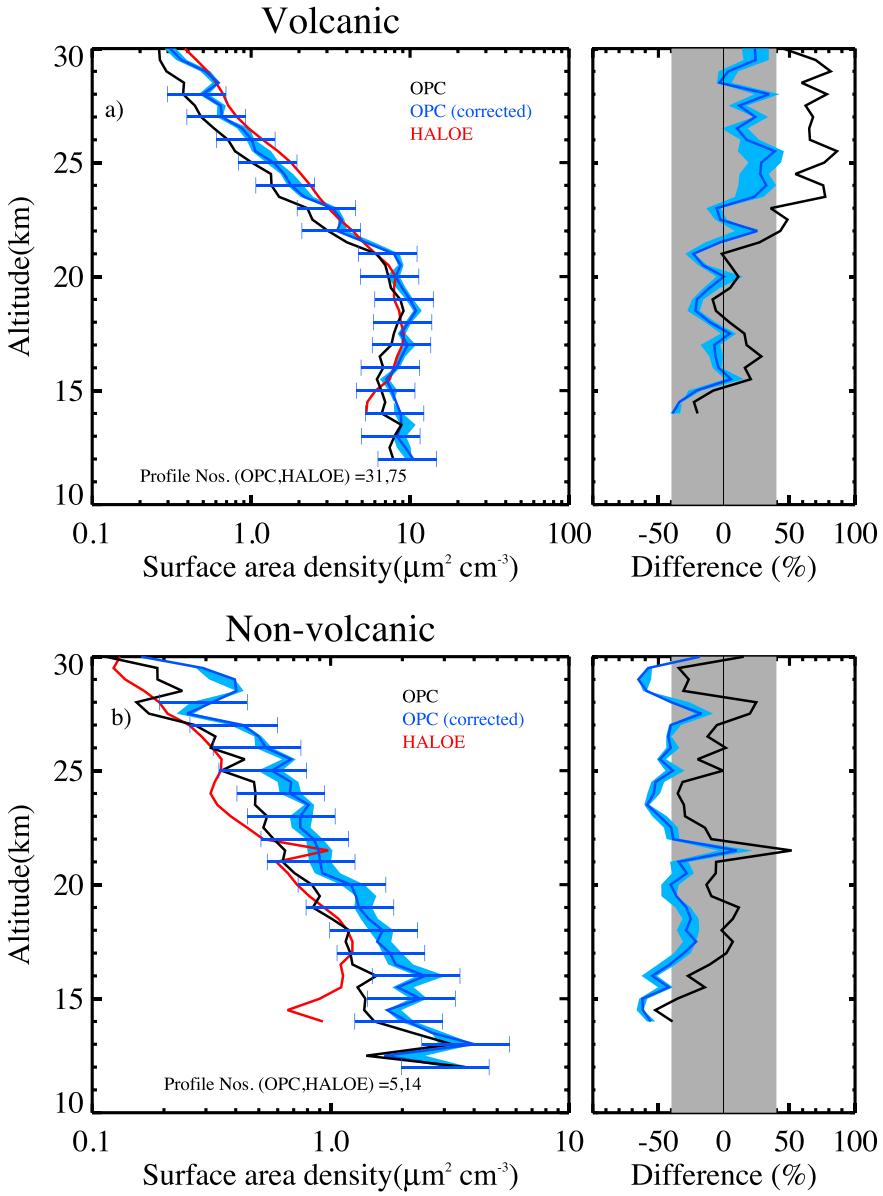

Figure 10. Average SAD profiles of OPC and HALOE for the (a) volcanic and (b) nonvolcanic periods. SAD_{HALOE} is shown in red, SAD_{OPCnc} in black, and SAD_{OPCwc} in blue. The SAD_{OPC} error bars represent ±40% precision in SAD. Blue shading represents the range of fdn_{ref}, bounding from $fdn_{ref} = 4$ to $fdn_{ref} = 10$. Grey shading represents the OPC precision range. Vertical profile of mean percentage difference $((SAD_{HALOE} - SAD_{OPC})/SAD_{OPC})$ is also shown for both SAD_{OPCnc} (black) and SAD_{OPCwc} (blue).

change significantly during the volcanic period, but the change is substantial during the nonvolcanic period, increasing by ~50%.

During the volcanic period (Figure 9a), $SAD_{SV6.2}$ is higher than SAD_{OPCnc}, throughout the stratosphere. Corrections to the OPC measurements bring SAD_{OPCwc} close to $SAD_{SV6.2}$. SAGE II SAD in the current operational version ($SAD_{SV7.0}$) is very close to $SAD_{SV6.2}$, with a deviation low at the bottom of the profile and high at the top, but overall SAD does not change significantly during volcanic period with the different data versions and different ways to calculate SAD [*Damadeo et al.*, 2013]. $SAD_{SV7.0}$ is in better agreement with SAD_{OPCnc}, at altitudes between 12 and 20 km but deviates to differences of 50–100% above 20 km. Between $SAD_{SV7.0}$ and SAD_{OPCwc} the agreement is improved above 20 km but worsens, with

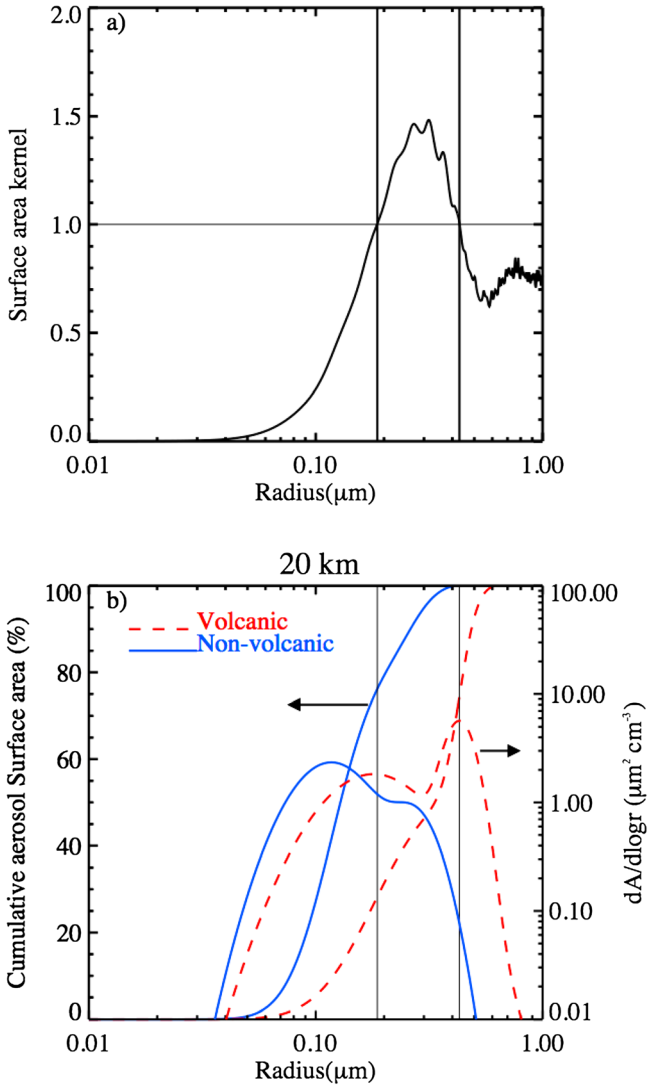

Figure 11. (a) Surface area kernel as a function of radius. Solid vertical lines bound the range for which the surface area is over estimated. (b) Differential (scale on the right) and cumulative (scale on the left) distribution of SAD in percentage at 20 km for nonvolcanic (solid blue lines) and volcanic (dotted red lines) case. Vertical lines same as in Figure 11a.

$SAD_{SV7.0} < SAD_{OPCwc}$ below 20 km. Still $SAD_{SV7.0}$ is primarily within the ±40% precision of SAD_{OPCwc} as is $SAD_{SV6.2}$.

For the nonvolcanic period, $SAD_{SV6.2}$ is predominantly a factor of 2 or more lower than the uncorrected SAD_{OPCnc}, which was previously documented [*Deshler et al.*, 2003a; *SPARC*, 2006; *Thomason et al.*, 2008]. This difference increases to a factor of 3 or more for $SAD_{SV6.2}$ compared to SAD_{OPCwc}, Figure 9b. The agreement is significantly better between $SAD_{SV7.0}$ and SAD_{OPC}, both uncorrected and corrected. $SAD_{SV7.0}$ is in quite good agreement with SAD_{OPCnc} between 15 and 20 km, while the agreement is significantly improved, with SAD_{OPCwc}. There are still significant disagreements below 15 km and above 28 km; however, $SAD_{SV7.0}$ is significantly improved throughout the stratosphere and is mostly within the measured uncertainty of the SAD_{OPCwc}.

SAD from HALOE is estimated by using HALOE extinction measurements at three wavelengths to retrieve unimodal lognormal size distribution parameters, N, r_m, and σ. [*Hervig et al.*, 1998; *Hervig and Deshler*, 2002]. Then, $SAD_{HALOE} = 4\pi r_m^2 N \exp(2\ln^2\sigma)$. Distribution width, σ, is inferred from effective radius (Re), which is calculated using 2.45 μm extinction measurements [*Hervig et al.*, 1998].

Figure 10 shows the comparison of SAD_{OPC} against HALOE (SAD_{HALOE}), for both volcanic and nonvolcanic periods. During the volcanic period, the agreement between SAD_{HALOE} and SAD_{OPCnc} is within 30–40%, up to 23 km. Above 23 km, $SAD_{HALOE} > SAD_{OPCnc}$ by 50–75%. The agreement improves when the OPC corrections are done and is within ±40% throughout the stratosphere. During the nonvolcanic period, SAD_{HALOE} is in quite good agreement with SAD_{OPCnc} up to 20 km, while SAD_{HALOE} is lower than SAD_{OPCnc} by 20–30% above 20 km. SAD_{HALOE} is $< SAD_{OPCwc}$ throughout the stratosphere, but overall SAD_{HALOE} is still within the ±40% precision of OPC_{SADwc}. The discrepancies between SAD_{HALOE} and SAD_{OPC} may be due to limitations in the retrieval of SAD_{HALOE} which is estimated from retrieved unimodal lognormal size distributions, using the 2.45 μm extinction measurements [*Hervig and Deshler*, 2002]. According to *Thomason* [2012], the 2.45 μm measurements are biased during volcanically quiescent periods.

It is known that $SAD_{SV6.2}$ underestimates SAD during nonvolcanic periods because SAGE II aerosol measurements are not sensitive to smaller particles, which contribute more toward SAD during nonvolcanic periods [*Deshler et al.*, 2003a; *SPARC*, 2006; *Thomason et al.*, 2008]. *Steele and Turco* [1997] pointed out that the SAGE II-measured extinctions decrease quickly as particles approach 0.1 μm

(Figure 6a), precisely the region where the aerosol concentration is still increasing for the nonvolcanic period. *Steele et al*. [1999] studied the source of the underestimation of SAGE II SAD during the background period and showed that from SAGE II, SAD can be estimated as

$$\mathrm{SAD_{est}} = \sum_i a_i\beta_i = \sum_i a_i \int \pi r^2 Q(\lambda_i, r)\frac{\mathrm{d}n}{\mathrm{d}r}\mathrm{d}r = \int \left(\underbrace{\sum_i a_i \frac{Q(\lambda_i, r)}{4}}_{\text{kernel approx.}} \right) \frac{\mathrm{d(SAD)}}{\mathrm{d}r}\mathrm{d}r, \tag{15}$$

where a_i are the coefficients obtained from the PCA analysis for the SAGE II wavelengths, β_i are the extinction measurements from SAGE II, and the summation is over all the SAGE II extinction wavelengths. If the kernel approximation in equation (15) is equal to 1, then the area estimated would be exact. Figure 11a shows the radius dependence of the SAD kernel $\left(\sum_i a_i \frac{Q(\lambda_i,r)}{4}\right)$, using a_i from *Steele et al*. [1999], indicating that SAD will be underestimated for particles less than 0.18 μm and for particles greater than 0.43 μm, while SAD between 0.18 μm and 0.43 μm is overestimated.

The differential and cumulative distributions of SAD provide the contribution of each radii range to the total SAD. Figure 11b compares the SAD kernel from equation (15) to differential and cumulative distributions of SAD for size distributions measured at 20 km for a nonvolcanic (20,000,412, blue solid line) and a volcanic (19,940,308, red dashed line) measurement. The OPC measurements used to construct Figure 11b are corrected for evaporation, anisokineticity, and counting efficiency. The solid vertical lines in Figure 11 bound the sizes when SAD is underestimated/overestimated by SAGE II. The figure depicts clearly the contribution of smaller particles to total SAD during nonvolcanic periods. The cumulative SAD for the nonvolcanic period shows that about 75% of the total SAD is contained in particles below 0.18 μm where SAD is underestimated according to equation (15), and only about 25% of the total SAD falls in the size range where SAD is overestimated. For the volcanic period, about 25% of the total SAD is contained in particles below 0.18 μm and 20% is contributed by particles larger than 0.3 μm. Thus, the contributions in the underestimation and overestimation regions are similar for volcanically disturbed stratospheric aerosol.

Figure 11 clearly indicates that during the nonvolcanic period, the underestimation of $\mathrm{SAD_{SV6.2}}$ arises because SAGE II is not sensitive to the small particles which contribute more toward the SAD during the background period, also concluded by *Thomason et al*. [2008]. $\mathrm{SAD_{SV6.2}}$ also underestimates the SAD reported from FCAS in situ measurements by about a factor of 1.5–3 [*Reeves et al*., 2008]. Clearly, there is significant improvement in $\mathrm{SAD_{SV7.0}}$, which in the nonvolcanic period shows a disagreement with $\mathrm{SAD_{SV6.2}}$ which is similar to the differences between $\mathrm{SAD_{SV6.2}}$ and in situ measurements [*Deshler et al*., 2003a; *Reeves et al*., 2008]. Thus, $\mathrm{SAD_{SV7.0}}$ will be in much better agreement with SAD from FCAS as it is with the corrected $\mathrm{SAD_{OPC}}$ described here.

4. Summary and Conclusions

Up to this point the long-term stratospheric aerosol measurements from the University of Wyoming OPC have been presented directly, without correction for particle evaporation, anisokineticity, and counting efficiency. Particle evaporation in the OPC inlet and anisokineticity of the inlet geometry have been considered in the past but found to be within larger uncertainties in the measurements and thus dismissed. Here for the first time, particle evaporation has been accounted for with a model of air temperature along the inlet; isokineticity has been considered formally and dismissed, and particle counting efficiency has been measured and applied to the measurements. Motivation for these considerations was provided by discrepancies between OPC estimates of extinction and SAGE II measurements, during nonvolcanic (low aerosol loading) periods.

The counting efficiency correction results from a systematic calibration error which crept into the measurements with the development of a higher flow rate, improved aerosol size range instrument developed in the late 1980s [*Hofmann and Deshler*, 1991]. The issue has to do with how each photodetector is calibrated when two photodetectors are used simultaneously to measure particle size. Applying a correction for this systematic counting efficiency error, however, is not straight forward. It depends on the shape of the aerosol number size distribution. Full counting efficiency corrections are

required for regions of the distribution where there are large changes in concentration between particle size bins but must be diminished when number concentrations change little between adjacent bins. Thus, the counting efficiency correction becomes more important during nonvolcanic periods when size distributions are narrower, than during volcanic periods when there is an abundance of larger particles and size distributions are broader. The counting efficiency corrections do not apply to the older, low flow rate, two-channel instruments used prior to the 1990s and sensitive only to particles less than 0.3 μm.

The evaporation of particles in the OPC inlet has a small effect, increasing the true size of the particles by 6–10% over their measured size. This increases derived aerosol moments by about 10–15% for all measurements. The counting efficiency correction has the major impact on the measurements, increasing aerosol moments by 15–25% during volcanic (high aerosol loading) periods and by 30–50% during nonvolcanic periods.

The primary quantity of interest for stratospheric aerosol is its surface area density (SAD) because of its impact on stratospheric chemistry and radiation. The evaporation of particles in the OPC inlet and anisokineticity has a small impact on SAD_{OPC}; however, the counting efficiency correction can be significant, depending on the size distribution. For the Mount Pinatubo volcanic period, the corrected OPC SADs increase by about 25%, improving the comparison with SAD estimates from SAGE II (version 6.2, $SAD_{sv6.2}$, and version 7.0, $SAD_{sv7.0}$). Differences are within the ±40% precision of SAD_{OPC}. Differences between $SAD_{sv6.2}$ and $SAD_{sv7.0}$ are small during volcanic periods. During the nonvolcanic period following Mount Pinatubo, the corrected OPC SADs increase by about 50%, further increasing the previous underestimation of $SAD_{SV6.2}$, from a factor of 2 or more, to a factor of 3 or more. An improved method developed by *Thomason et al.* [2008], to calculate $SAD_{SV7.0}$, is in significantly better agreement with the corrected SAD_{OPC} except below 15 and above 28 km.

Differential and cumulative distributions of SAD clearly show that for low aerosol loading measurements, the underestimation of $SAD_{SV6.2}$ arises because SAGE II is not sensitive to the smaller particles, which, in these cases, are the largest contributors to SAD. The small particles are also more sensitive to the OPC counting efficiency correction during low aerosol loading. The maximum SAD estimated using Method 1 in *Thomason et al*. [2008] does a reasonable job of accounting for this deficiency and produces values comparable to SAD_{OPC}, with appropriate corrections, during the nonvolcanic period. This method, however, does not apply for volcanic periods where the principal component analysis used in $SAD_{SV6.2}$ does a better job. $SAD_{SV7.0}$ is adjusted to approach $SAD_{SV6.2}$ as aerosol loading increases, following volcanic activity, when the 1.02 μm extinction approaches 70% of the 0.525 μm extinction.

These changes significantly improve the agreement of the Wyoming OPC-derived aerosol extinctions compared with SAGE II and HALOE measurements during nonvolcanic periods, while slightly degrading the agreement during volcanic periods. Aerosol surface area density from the corrected OPC remains in agreement with SAGE II $SAD_{SV6.2}$ during the volcanic period, while leading to a larger discrepancy with $SAD_{SV6.2}$ during the nonvolcanic period. $SAD_{SV7.0}$ changes this agreement during the volcanic period only slightly, while significantly improving the agreement with the corrected SAD_{OPC} for nonvolcanic periods.

Acknowledgments
The stratospheric measurements from Laramie have been supported by several agencies over the years, most notably the U.S. National Science Foundation, which is supporting the current work under grant ATM-1011827. Many people from the Department of Atmospheric Science are, and have been, involved in the bimonthly balloon flights from Laramie. We appreciate their effort and acknowledge their contribution toward the quality of these measurements. We also thank the SAGE II science team for the SAGE II measurements. SAGE II data used in this study are downloaded from https://eosweb.larc.nasa.gov/project/sage2/sage2_table. HALOE data are downloaded from http://haloe.gats-inc.com/home/index.php. OPC measurements are available at http://www-das.uwyo.edu/~deshler/Data/Aer_Meas_Wy_read_me.htm.

References

Adriani, A., T. Deshler, G. D. Donfrancesco, and G. P. Gobbi (1995), Polar stratospheric clouds and volcanic aerosol during spring 1992 over McMurdo Station, Antarctica: Lidar and particle counter comparisons, *J. Geophys. Res.*, *100*(D12), 25,877–25,897, doi:10.1029/95JD02029.

Belyaev, S. P., and L. M. Levin (1974), Techniques for collection of representative aerosol samples, *J. Aerosol Sci.*, *5*, 713–720.

Campbell, P., and T. Deshler (2014), Condensation nuclei measurements in the midlatitude (1982–2012) and Antarctic (1986–2010) stratosphere between 20 and 35 km, *J. Geophys. Res. Atmos.*, *119*, 137–152, doi:10.1002/2013JD019710.

Chu, W. P., M. P. McCormick, J. Lenoble, C. Brogniez, and P. Pruvost (1989), SAGE II inversion algorithm, *J. Geophys. Res.*, *94*(D6), 8339–8351, doi:10.1029/JD094iD06p08339.

Clegg, S. L., P. Brimblecombe, and A. S. Wexler (1998), A thermodynamic model of the system H^+-NH_4^+-SO_4^{2-}-NO_3^--H_2O at tropospheric temperatures, *J. Phys. Chem.*, *102A*, 2137–2154.

Damadeo, R. P., J. M. Zawodny, L. W. Thomason, and N. Iyer (2013), SAGE version 7.0 algorithm: Application to SAGE II, *Atmos. Meas. Tech. Discuss.*, *6*, 5101–5171, doi:10.5194/amtd-6-5101-2013.

Deshler, T., B. J. Johnson, and W. R. Rozier (1993), Balloonborne measurements of Pinatubo aerosol during 1991 and 1992 at 41°N, vertical profiles, size distribution, and volatility, *Geophys. Res. Lett.*, *20*, 1435–1438.

Deshler, T., B. Nardi, A. Adriani, F. Cairo, G. Hansen, F. Fierli, A. Hauchecorne, and L. Pulvirenti (2000), Determining the index of refraction of polar stratospheric clouds above Andoya (69°N) by combining size-resolved concentration and optical scattering measurements, *J. Geophys. Res.*, *105*(D3), 3943–3953, doi:10.1029/1999JD900469.

Deshler, T., M. E. Hervig, D. J. Hofmann, J. M. Rosen, and J. B. Liley (2003a), Thirty years of in situ stratospheric aerosol size distribution measurements from Laramie, Wyoming (41°N) using balloon-borne instruments, *J. Geophys. Res.*, *108*(D5), 4167, doi:10.1029/2002JD002514.

Deshler, T., et al. (2003b), Large nitric acid particles at the top of an Arctic stratospheric cloud, *J. Geophys. Res.*, *108*(D16), 4517, doi:10.1029/2003JD003479.
Deshler, T., R. Anderson-Sprecher, H. Jager, J. Barnes, D. J. Hofmann, B. Clemesha, D. Simonich, M. Osborn, R. G. Grainger, and S. Godin-Beekmann (2006), Trends in the nonvolcanic component of stratospheric aerosol over the period 1971–2004, *J. Geophys. Res.*, *111*, D01201, doi:10.1029/2005JD006089.
Eidhammer, T., and T. Deshler (2005), Technical note: Evaporation of polar stratospheric cloud particles, in situ, in a heated inlet, *Atmos. Chem. Phys.*, *5*, 97–106.
Eidhammer, T., D. C. Montague, and T. Deshler (2008), Determination of index of refraction and size of supermicrometer particles from light scattering measurements at two angles, *J. Geophys. Res.*, *113*, D16206, doi:10.1029/2007JD009607.
Fahey, D. W., et al. (1993), In situ measurements constraining the role of sulphate aerosols in mid-latitude ozone depletion, *Nature*, *363*, 509.
Fuchs, N., and A. Sutugin (1971), *Highly Dispersed Aerosols, in Topics in Current Aerosol Research*, Pergamon Press, New York.
Gmitro, J. I., and T. Vermeulen (1964), Vapor–liquid equilibria for aqueous sulfuric acid, *AIChE J.*, *10*, 740–746.
Granqvist, C. G., and R. A. Buhrman (1976), Log-normal size distributions of ultrafine metal particles, *Solid State Commun.*, *18*, 123–126.
Hervig, M. E., and T. Deshler (2002), Evaluation of aerosol measurements from SAGE II, HALOE, and balloonborne optical particle counters, *J. Geophys. Res.*, *107*(D3), 4031, doi:10.1029/2001JD000703.
Hervig, M. E., T. Deshler, and J. M. Russell III (1998), Aerosol size distributions obtained from HALOE spectral extinction measurements, *J. Geophys. Res.*, *103*, 1573–1583, doi:10.1029/97JD03081.
Hofmann, D. J. (1990), Increase in the stratospheric background sulfuric acid aerosol mass in the past 10 years, *Science*, *248*, 996–1000.
Hofmann, D. J., and T. Deshler (1991), Stratospheric cloud observations during formation of the Antarctic ozone hole in 1989, *J. Geophys. Res.*, *96*, 2897–2912, doi:10.1029/90JD02494.
Hofmann, D. J., and S. J. Oltmans (1992), The effect of stratospheric water vapor on the heterogeneous reaction rate of $ClONO_2$ and H_2O for sulfuric acid aerosol, *Geophys. Res. Lett.*, *19*(22), 2211–2214, doi:10.1029/92GL02493.
Hofmann, D. J., and J. M. Rosen (1983), Sulfuric acid droplet formation and growth in the stratosphere after the 1982 eruption of El Chichón, *Science*, *222*, 325–327.
Hofmann, D. J., and S. Solomon (1989), Ozone depletion through heterogeneous chemistry following the eruption of the El Chichon Volcano, *J. Geophys. Res.*, *94*, 5029–5041, doi:10.1029/JD094iD04p05029.
Hofmann, D. J., J. M. Rosen, T. J. Pepin, and R. G. Pinnick (1975), Stratospheric aerosol measurements: 1. Time variations at northern midlatitudes, *J. Atmos. Sci.*, *32*, 1446–1456.
Jäger, H. (2005), Long-term record of lidar observations of the stratospheric aerosol layer at Garmisch-Partenkirchen, *J. Geophys. Res.*, *110*, D08106, doi:10.1029/2004JD005506.
Jäger, H., and D. Hofmann (1991), Midlatitude lidar backscatter to mass, area, and extinction conversion model based on in situ aerosol measurements from 1980 to 1987, *Appl. Opt.*, *30*, 127–138.
Kovilakam, M. (2012), On the accuracy of stratospheric aerosol extinction and surface area derived from in situ and remote measurements, PhD dissertation, Dep. of Atmos. Sci., Univ. of Wyoming, Laramie.
Luo, B., U. Krieger, and T. Peter (1996), Densities and refractive indices of $H_2SO_4/HNO_3/H_2O$ solutions to stratospheric temperatures, *Geophys. Res. Lett.*, *23*, 3707–3710, doi:10.1029/96GL03581.
Mauldin, L. E., III, N. H. Zaun, M. P. McCormick, J. H. Guy, and W. R. Vaughan (1985), Stratospheric aerosol and gas experiment II instrument: A functional description, *Opt. Eng.*, *24*, 307–312.
Miao, Q. (2001), An analysis of errors associated with the measurement of aerosol concentration in situ with optical particle counters, MS thesis, 71 pp., Univ. of Wyoming, Laramie.
Minnis, P., E. F. Harrison, L. L. Stowe, G. G. Gison, F. M. Denn, D. R. Doelling, and W. L. Smith Jr. (1993), Radiative climate forcing by the Mount Pinatubo eruption, *Science*, *259*, 1411–1415.
Niedziela, R. F., M. L. Norman, R. E. Miller, and D. R. Worsnop (1998), Temperature- and composition-dependent infrared optical constants for sulfuric acid, *Geophys. Res. Lett.*, *25*, 4477–4480, doi:10.1029/1998GL900202.
Palmer, K. F., and D. Williams (1975), Optical constants of sulfuric acid: Application to the clouds of Venus?, *Appl. Opt.*, *14*, 208–219.
Pruppacher, H., and J. Klett (1997), *Microphysics of Clouds and Precipitation*, Kluwer Acad., Dordrecht, Netherlands.
Pueschel, R. F., K. G. Snetsinger, P. B. Russell, S. A. Kinne, and J. M. Livingston (1992), The effects of the 1991 Pinatubo volcanic eruption on the optical and physical properties of stratospheric aerosols, in *Proceedings of IRS92: Current Problems in Atmospheric Radiation*, edited by S. Keevalik, pp. 183–186, A. Deepak, Hampton, Va.
Pueschel, R. F., B. Russell, D. A. Allen, G. V. Ferry, and K. G. Snetsinger (1994), Physical and optical properties of the Pinatubo volcanic aerosol: Aircraft observations with impactors and a Sun-tracking photometer, *J. Geophys. Res.*, *99*, 12,915–12,922, doi:10.1029/94JD00621.
Reeves, J. M., J. C. Wilson, C. A. Brock, and T. P. Bui (2008), Comparison of aerosol extinction coefficients, surface area density, and volume density from SAGE II and in situ aircraft measurements, *J. Geophys. Res.*, *113*, DI1202, doi:10.1029/2007JD009357.
Ridley, D. A., et al. (2014), Total volcanic stratospheric aerosol optical depths and implications for global climate change, *Geophys. Res. Lett.*, *41*, 7763–7769, doi:10.1002/2014GL061541.
Rodriguez, J. M., M. K. W. Ko, and N. D. Sze (1991), Role of heterogeneous conversion of N_2O_5 on sulfate aerosols in global ozone loss, *Nature*, *352*, 134–137.
Rosen, J. M. (1964), The vertical distribution of dust to 30 km, *J. Geophys. Res.*, *69*, 4673–4676, doi:10.1029/JZ069i021p04673.
Rosen, J. M. (1971), The boiling point of stratospheric aerosols, *J. Appl. Meteorol.*, *10*, 1044–1046.
Rosen, J. M., and D. J. Hofmann (1977), Balloonborne measurements of condensation nuclei, *J. Appl. Meteorol.*, *16*, 56–62.
Russell, J. M., III, L. L. Gordley, J. H. Park, S. R. Drayson, W. D. Hesketh, R. J. Cicerone, A. F. Tuck, J. E. Frederick, J. E. Harries, and P. J. Crutzen (1993), The halogen occultation experiment, *J. Geophys. Res.*, *98*, 10,777–10,797, doi:10.1029/93JD00799.
Russell, P. B., et al. (1996), Global to microscale evolution of the Pinatubo volcanic aerosol derived from diverse measurements and analyses, *J. Geophys. Res.*, *101*(D13), 18,745–18,763, doi:10.1029/96JD01162.
Solomon, S., R. W. Portman, R. R. Garcia, L. W. Thomason, L. R. Poole, and M. P. McCormick (1996), The role of aerosol variability in anthropogenic ozone depletion at northern midlatitudes, *J. Geophys. Res.*, *101*, 6713–6727, doi:10.1029/95JD03353.
Steele, H. M., and P. Hamill (1981), Effects of temperature and humidity on the growth and optical properties of sulphuric acid-water droplets in the stratosphere, *J. Aerosol Sci.*, *12*, 517–528.
Steele, H. M., and R. P. Turco (1997), Retrieval of aerosol size distributions from satellite extinction spectra using constrained linear inversion, *J. Geophys. Res.*, *102*, 16,737–16,747, doi:10.1029/97JD01264.
Steele, H. M., J. D. Lumpe, R. P. Turco, R. M. Bevilacqua, and S. T. Massie (1999), Retrieval of aerosol surface area and volume densities from extinction measurements: Application to POAM II and SAGE II, *J. Geophys. Res.*, *104*, 9325–9336, doi:10.1029/1999JD900032.

Stratospheric Processes and their Role in Climate (SPARC): Assessment of stratospheric aerosol properties (ASAP) (2006), Technical report WCRP-124/WMO/TD-No. 1295/SPARC report no. 4, SPARC. [Available at http://www.sparc-climate.org/publications/sparc-reports/sparc-report-no4/.]

Tabazadeh, A., S. Martin, and J. Lin (2000), The effect of particle size and nitric acid uptake on the homogeneous freezing of aqueous sulfuric acid particles, *Geophys. Res. Lett.*, *27*, 111–1114.

Thomason, L. W. (2012), Toward a combined SAGEII-HALOE aerosol climatology: an evaluation of HALOE version 19 stratospheric aerosol extinction coefficient observations, *Atmos. Chem. Phys.*, *12*, 8177–8188.

Thomason, L. W., L. R. Poole, and T. Deshler (1997), A global climatology of stratospheric aerosol surface area density as deduced from SAGE II: 1984–1994, *J. Geophys. Res.*, *102*, 8967–8976, doi:10.1029/96JD02962.

Thomason, L. W., et al. (2008), SAGE II measurements of stratospheric aerosol properties at non-volcanic levels, *Atmos. Chem. Phys.*, *8*, 983–995.

Wang, P. H., M. P. McCormick, L. R. Poole, W. P. Chu, G. K. Yue, G. S. Kent, and K. M. Skeens (1994), Tropical high cloud characteristics derived from SAGE II extinction measurements, *Atmos. Res.*, *34*, 53–83.

Wilson, J. C., et al. (2008), Steady-state aerosol distributions in the extra-tropical, lower stratosphere and the processes that maintain them, *Atmos. Chem. Phys.*, *8*, 6617–6626, doi:10.5194/acp-8-6617-2008.

World Meteorological Organization (2003), Scientific Assessment of Ozone Depletion: 2002, *Global Ozone Research and Monitoring Project—Rep.*, *47*, 498 pp., Geneva.

Xu, R. (2001), *Particle Characterization: Light Scattering Methods*, Kluwer Acad., Dordrecht, Netherlands.